ON THE DESIGN OF TRANSFERS TO SOLAR-SAIL DISPLACED ORBITS IN THE EARTH-MOON SYSTEM

Thomas D. van den Oever and Jeannette Heiligers

Delft University of Technology, Delft, The Netherlands

ABSTRACT

This paper presents the design of solar-sail transfer trajectories to solar-sail displaced libration point orbits in the Earth-Moon system. The existence of families of solar-sail displaced libration point orbits in the Earth-Moon system has recently been demonstrated. These families originate from complementing the dynamics of the classical Earth-Moon circular restricted three-body problem with a solar-sail induced acceleration. Previous work has furthermore demonstrated the applicability of these orbits for high-latitude observation of the Earth and Moon. To not only demonstrate the existence and applicability of these orbits, but also their accessibility, this paper investigates the design of solar-sail transfers from Earth-bound parking orbits to a subset of these orbits. Initial guesses for the transfers are generated using reverse time propagation of the dynamics, where the control is provided by a locally optimal steering law. These initial guesses are subsequently used to initialize a 12^{th}-order Gauss-Lobatto collocation method to satisfy a large number of constraints: departure from specific high Earth orbits, a minimum altitude with respect to the Earth and the Moon, and a maximum rotation rate of the solar sail. As an application of the developed methodology, this paper shows results for transferring two spacecraft to a constellation of displaced vertical Lyapunov orbits at the Earth-Moon L_2 point. This constellation has been shown to provide continuous coverage of the lunar Aitken Basin and the lunar South Pole while maintaining a continuous line of sight with Earth. Sets of feasible trajectories for both spacecraft with identical launch conditions are produced in order for the constellation to be initiated using a single Soyuz launch. Such a Soyuz launch can deliver two 1160-kg spacecraft into the found transfer trajectories. One of the spacecraft subsequently requires a transfer time of 53.06 days to enter its constellation orbit, while the transfer of the other spacecraft takes 67.89 days. These results prove the accessibility of solar-sail displaced libration point orbits in the Earth-Moon system, thereby reaffirming the potential of solar-sail technology to enable novel scientific missions in the Earth-Moon system.

Index Terms— Solar sailing, libration points, Earth-Moon system, locally optimal steering laws, collocation

1. INTRODUCTION

Recent developments in solar-sail technology [1, 2, 3] grant opportunities for the advancement of new mission concepts. The advantage of employing a solar sail is that a continuous acceleration can be provided without the need for a mass-consuming propulsion system [4]. This allows for new types of non-Keplerian orbits in two-body systems, e.g., around Earth or the Sun [4], and in three-body systems, e.g., in the Sun-Earth system, see, for example, Refs. [4, 5, 6, 7]. Moreover, recent work [8, 9] has demonstrated the existence of families of solar-sail displaced libration point orbits in the Earth-Moon system. These families originate from complementing the dynamics of the classical Earth-Moon circular restricted three-body problem with a solar-sail induced acceleration. The addition of this acceleration makes the problem non-autonomous, but by constraining the orbital period in a differential correction scheme, closed orbits can be found that are periodic with the Sun's synodic motion about the Earth-Moon system. These orbits can then be cataloged into traditional orbit families such as solar-sail displaced Lyapunov, halo, and vertical Lyapunov orbits where different families can be generated for different solar-sail steering laws. Previous work has also demonstrated the applicability of these orbits for high-latitude observation of the Earth and Moon [10]. For example, orbits from within the family of solar-sail displaced vertical Lyapunov orbits at the L_2 point [10], can be used to provide continuous coverage of interesting features on the Moon, including the Aitken Basin and the lunar South Pole. The Aitken Basin is scientifically interesting as it reveals deeper layers of the lunar crust [11]. Also, the far-side of the Moon is a perfect site for a radio-telescope as it is continuously shielded from Earth-based radio noise and can thus study signals that can otherwise not be detected [11]. Finally, in the future, the lunar South Pole may host a permanent human outpost as it is continuously lit by sunlight, which provides power, and because water ice is believed to exist in its permanently shadowed lunar craters [11]. For these proposed lunar mission concepts, a continuous communication link between the lunar surface, the spacecraft and Earth is required. When using a constellation of two spacecraft in such solar-sail displaced L_2 vertical Lyapunov orbits, continuous coverage of the Aitken Basin and the lunar South Pole can be provided, while maintaining a permanent view of the Earth [10].

To not only demonstrate the existence and applicability of these orbits, but also their accessibility, this paper proposes a methodology to design solar-sail transfers from Earth-bound orbits to solar-sail displaced libration point orbits in the Earth-Moon system. This will enable an assessment of the mission performance in terms of achievable transfer times and deliverable spacecraft (payload) mass. Previous solar-sail transfer trajectories have been designed using locally optimal steering laws, e.g., Ref. [12], including transfers in the Earth-Moon system [13], or using the velocity tangent steering law refined with collocation techniques [14]. These methods result in trajectories connecting a parking orbit such as geostationary transfer orbit with a target orbit in the Earth-Moon system, but require rapid changes in the sail attitude and long transfer times. To further improve the design of solar-sail transfer trajectories, this paper develops a collocation method with a range of additional path and point constraints.

Initial guesses for these transfers are generated by reverse time propagation of the dynamics in the solar-sail augmented circular restricted three-body problem, where the solar-sail control law is provided by a locally optimal steering law. In order to enforce constraints on the found trajectories, the 12^{th}-order Gauss-Lobatto collocation method is applied to transcript the trajectory to a nonlinear programming (NLP) problem [15, 16]. Collocation methods can incorporate path and point constraints and, contrary to, for example, multiple shooting methods, do not require an explicit integration of the dynamics. Collocation methods also have a wider radius of convergence than multiple shooting methods, as the sensitivity of the trajectory is distributed over more segments [17]. In order to improve the radius of convergence and accuracy even further, an error estimation scheme based on Ref. [18] is applied in order to refine the mesh and equidistribute the error. Consecutively, the NLP-problem is solved using the multivariate Gauss-Newton algorithm [19] in conjunction with a line search method [17].

This paper applies the proposed methodology to obtain transfer trajectories to the previously mentioned constellation of solar-sail displaced L_2 vertical Lyapunov orbits where two spacecraft are launched with a single Soyuz launch vehicle into a highly elliptic Earth orbit from where the transfers towards the L_2 region are initiated. Once the trajectory for one of the spacecraft is found, a similar trajectory with identical launch conditions is sought for the second spacecraft. Finally, to assess the mission performance in terms of spacecraft (payload) mass budget, a preliminary mass budget is constructed based on reference satellite data.

2. DYNAMICS

The dynamics of the solar-sail spacecraft are modelled in the framework of the Earth-Moon circular restricted three-body problem (CR3BP), taking into account the gravity of the Earth and Moon, as well as the solar radiation pressure (SRP) acting on the solar sail. This section will first discuss the dynamics of the CR3BP, followed by a model for the solar-sail acceleration. Since this acceleration is dependent on the instantaneous position of the Sun with respect to the Earth-Moon system, this section ends with a discussion on how the Sun's motion around the Earth-Moon system is modeled.

2.1. Circular restricted three-body problem

To express the dynamics in the CR3BP, it is convenient to define a synodic reference frame, SYN($\hat{\mathbf{x}}_{SYN}, \hat{\mathbf{y}}_{SYN}, \hat{\mathbf{z}}_{SYN}$), shown in Fig. 1, where the origin is located at the Earth-Moon barycenter, the $\hat{\mathbf{x}}_{SYN}$-axis is aligned with the Earth-Moon line, and the $\hat{\mathbf{z}}_{SYN}$ is oriented perpendicular to the Earth-Moon orbital plane, coinciding with the rotational direction of the reference frame, $\boldsymbol{\omega}_{rot}$. Finally, the $\hat{\mathbf{y}}_{SYN}$-axis completes the right-handed reference frame.

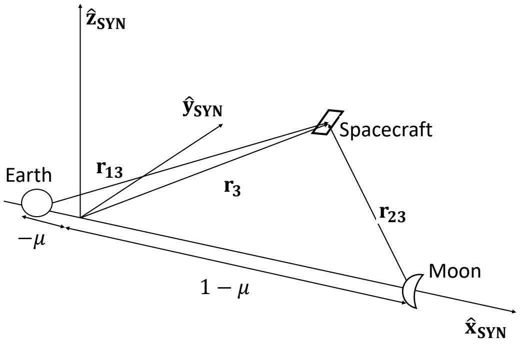

Fig. 1. Schematic of synodic reference frame.

It is furthermore convenient to use a set of canonical units. Distances are made dimensionless by taking the Earth-Moon distance as the unit of length, U_{length}. This results in the Earth being located at $\mathbf{r}_1 = [-\mu_{EM} \quad 0 \quad 0]^T$ and the Moon at $\mathbf{r}_2 = [1-\mu_{EM} \quad 0 \quad 0]^T$, where the mass fraction μ_{EM} is defined as

$$\mu_{EM} = \frac{m_2}{m_1 + m_2} \tag{1}$$

with m_1 and m_2 the masses of the Earth and Moon, respectively. Similarly, the time unit, U_{time}, is scaled such that the period of the Earth-Moon system equals 2π. Values for these units and parameters needed to model the Earth-Moon system can be found in Table 1.

The framework of the CR3BP exists under a set of assumptions: the Earth and Moon are assumed to be point masses, the orbits of the Earth and Moon are assumed to be coplanar and circular around their common barycenter, and the mass of the spacecraft, m_3, is assumed much smaller than the masses of the Earth and the Moon such that $m_3/m_1 \approx m_3/m_2 \approx 0$. Using these assumptions, the equations of motion of the spacecraft in the SYN-frame are given

Table 1. Parameters for the Earth-Moon CR3BP [20].

Parameter	Value	Unit	Description
m_1	$5.9723 \cdot 10^{24}$	kg	Mass Earth
m_2	$0.07346 \cdot 10^{24}$	kg	Mass Moon
μ_{EM}	0.01215	-	CR3BP mass fraction
r_{12}	$0.3844 \cdot 10^{6}$	km	Earth-Moon distance
P_M	27.4520	days	Period of the Moon around Earth
U_{length}	$0.3844 \cdot 10^{6}$	km	Distance unit
U_{time}	$0.3775 \cdot 10^{6}$	s	Time unit

by [21]:

$$\ddot{\mathbf{r}}_3 + 2\boldsymbol{\omega}_{rot} \times \dot{\mathbf{r}}_3 = -\nabla U(\mathbf{r}_3) + \mathbf{a}(t), \tag{2}$$

where $\mathbf{r}_3 = \begin{bmatrix} x_3 & y_3 & z_3 \end{bmatrix}^T$ is the position vector of the solar sail in the SYN-frame, $\boldsymbol{\omega}_{rot}$=$\begin{bmatrix} 0 & 0 & 1 \end{bmatrix}^T$ is the rotation vector of the SYN-frame and $\mathbf{a}(t)$ accounts for any additional acceleration terms; in this paper, the solar-sail induced acceleration. U is the sum of the gravitational and centripetal potentials given by:

$$U(\mathbf{r}_3) = -\frac{1-\mu_{EM}}{|\mathbf{r}_{13}|} - \frac{\mu_{EM}}{|\mathbf{r}_{23}|} - \frac{x_3^2 + y_3^2}{2}, \tag{3}$$

$$\mathbf{r}_{13} = \mathbf{r}_3 + \begin{bmatrix} \mu_{EM} & 0 & 0 \end{bmatrix}^T, \tag{4}$$

and

$$\mathbf{r}_{23} = \mathbf{r}_3 - \begin{bmatrix} 1-\mu_{EM} & 0 & 0 \end{bmatrix}^T, \tag{5}$$

where $\mathbf{r}_{13}$ and $\mathbf{r}_{23}$ are the position vectors of the spacecraft with respect to the Earth and the Moon. Equation 2 can be rewritten as a set of first-order differential equations $\frac{d\mathbf{x}}{dt} = \mathbf{f}(t, \mathbf{x}(t), \mathbf{a}(t))$ with $\mathbf{x}$ the state vector, $\mathbf{x} = \begin{bmatrix} \mathbf{r}_3^T & \dot{\mathbf{r}}_3^T \end{bmatrix}^T$, which can be explicitly integrated if the solar-sail acceleration in the term $\mathbf{a}(t)$ is known.

2.2. Solar-sail acceleration

The momentum carried by solar photons can be exchanged with an object by reflecting, absorbing and re-radiating these photons. This principle can be exploited as a propulsion method by utilizing a large, thin, highly reflective surface called a solar sail [4]. In this work, the solar sail is assumed to be an ideal reflector, where every photon is reflected specularly. In that case, the acceleration generated by the sail acts perpendicular to the sail membrane. The resulting acceleration is therefore a function of the orientation of the sail. In order to describe this orientation with respect to the Sun, a new Sun-sail fixed reference frame, SSF$\left(\hat{\mathbf{r}}_{43}, \hat{\boldsymbol{\theta}}_{43}, \hat{\boldsymbol{\varphi}}_{43}\right)$, is defined, see Fig. 2 [22]. The $\hat{\mathbf{r}}_{43}$-axis is defined along the incoming SRP direction:

$$\hat{\mathbf{r}}_{43} = \frac{\mathbf{r}_{43}}{|\mathbf{r}_{43}|}. \tag{6}$$

The other two axes, $\hat{\boldsymbol{\theta}}_{43}$ and $\hat{\boldsymbol{\varphi}}_{43}$, are defined as:

$$\hat{\boldsymbol{\theta}}_{43} = \frac{\hat{\mathbf{z}} \times \hat{\mathbf{r}}_{43}}{|\hat{\mathbf{z}} \times \hat{\mathbf{r}}_{43}|}, \tag{7}$$

with $\hat{\mathbf{z}} = \begin{bmatrix} 0 & 0 & 1 \end{bmatrix}^T$ and

$$\hat{\boldsymbol{\varphi}}_{43} = \hat{\mathbf{r}}_{43} \times \hat{\boldsymbol{\theta}}_{43}. \tag{8}$$

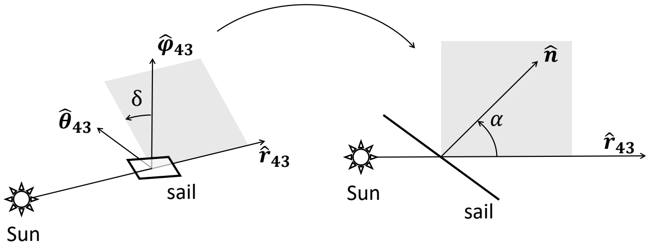

Fig. 2. Schematic of Sun-sail fixed reference frame, adapted from [22].

The orientation of the sail normal with respect to the SSF-frame can be defined by two angles: the cone and clock angles, α and δ, respectively, see Fig. 2. Note that, as the solar-sail cannot produce an acceleration component in the direction of the Sun, the domain of the cone angle is limited to 0 deg $\leq \alpha \leq$ 90 deg. The normal vector in the SSF-frame is then given by:

$$\hat{\mathbf{n}}_{SSF} = R_1(-\delta) R_2(-\alpha) \begin{bmatrix} 1 & 0 & 0 \end{bmatrix}^T,$$

where $R_j(\Psi)$ is a clockwise rotation matrix of angle Ψ around the 'j^{th}'-axis of a right-handed reference frame. Equation 2.2 can be written as

$$\hat{\mathbf{n}}_{SSF} = \begin{bmatrix} \cos(\alpha) & \sin(\alpha)\sin(\delta) & \sin(\alpha)\cos(\delta) \end{bmatrix}]^T.$$

To express this normal vector in the SYN-frame, the following rotation is applied:

$$\hat{\mathbf{n}}_{SYN} = \begin{bmatrix} [\hat{\mathbf{r}}_{43}]_{SYN} & [\hat{\theta}_{43}]_{SYN} & [\hat{\varphi}_{43}]_{SYN} \end{bmatrix} \hat{\mathbf{n}}_{SSF} \tag{9}$$

The solar-sail acceleration can then be computed from [4]:

$$\mathbf{a}(t) = a_{0,EM} (\hat{\mathbf{r}}_{43} \cdot \hat{\mathbf{n}}_{SYN})^2 \hat{\mathbf{n}}_{SYN}. \tag{10}$$

The characteristic solar-sail acceleration, $a_{0,EM}$, is the maximum achievable solar-sail acceleration for a given spacecraft mass and solar sail size. In this paper, a value for $a_{0,EM}$ of 0.1 (dimensionless units) is adopted, following the analyses in Ref. [10], see also Section 3.1. It is assumed that the spacecraft mass, solar sail size and solar radiation pressure in the Earth-Moon system are all constant, resulting in a constant $a_{0,EM}$. If the position of the Sun with respect to the SYN-frame, $\mathbf{r}_4$, is known the solar-sail acceleration can be calculated from Eq. 10.

2.3. Motion of the Sun

The Earth-Moon system orbits around the Sun, which causes the direction of the SRP in the synodic reference frame to change over time. In this work, it is assumed that the orbit of the Earth-Moon barycenter around the Sun is circular and that it is coplanar with the Earth-Moon orbital plane. This results in a clockwise, circular motion of the Sun in the $(\hat{\mathbf{x}}_{SYN}, \hat{\mathbf{y}}_{SYN})$-plane around the Earth-Moon barycenter [10], see Fig. 3.

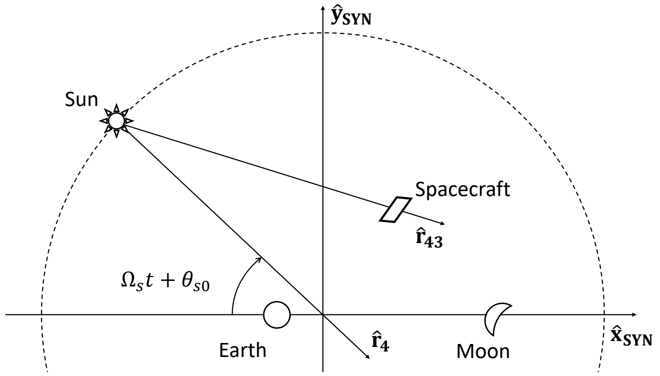

Fig. 3. Schematic of the position of the Sun with respect to the SYN-frame.

The position of the Sun is determined by the angular progression of the Moon around Earth and the angular progression of the Earth around the Sun. Therefore, the synodic angular velocity of the Sun, Ω_S, is used to determine the position of the Sun as a function of time, which is calculated using:

$$P_{syn} = \frac{1}{\frac{1}{P_M} - \frac{1}{P_E}} \tag{11}$$

and

$$\Omega_S = \frac{2\pi}{P_{syn}}. \tag{12}$$

The periods of Earth's orbit around the Sun, P_E, and the Moon's orbit around the Earth, P_M, are provided in Table 2. The orientation of the Sun with respect to the SYN-frame can then be described with [10]:

Table 2. Periods and angular velocities of the orbits of the Earth, Moon and Sun [20].

Parameter	Values	Unit	Description
P_E	365.256	days	Orbital period Earth
P_M	27.3217	days	Orbital period Moon
P_{syn}	29.5306	days	Sun's synodic period
Ω_S	0.9252	rad/-	Dimensionless angular rate of the Sun in the SYN-frame

$$\hat{\mathbf{r}}_4 = \begin{bmatrix} \cos(\Omega_s t + \theta_{s,0}) & -\sin(\Omega_s t + \theta_{s,0}) & 0 \end{bmatrix}^T, \tag{13}$$

where $\theta_{s,0}$ is the angular progression of the Sun at $t = 0$ since the last full Moon. In this work, it is assumed that the distances in the Earth-Moon system are small with respect to the Sun-Earth distance, resulting in: $\hat{\mathbf{r}}_{34} \approx \hat{\mathbf{r}}_4$. With $\hat{\mathbf{r}}_{43}$ known from $\hat{\mathbf{r}}_4$, the solar-sail acceleration in Eq. 10 can be evaluated for a given normal vector, $\hat{\mathbf{n}}_{SYN}$. If then a steering law for the sail is assumed, the differential equations in Eq. 2 can be integrated to find the corresponding solar-sail trajectory.

3. PROBLEM DESCRIPTION

As highlighted in the introduction, this paper searches for transfers between an Earth-based parking orbit and solar-sail displaced libration point orbits, in particular a constellation of two solar-sail displaced vertical Lyapunov orbits at the L_2 point. In this section, these departure and arrival conditions are discussed as a general layout of the transfer trajectory.

3.1. Solar-sail displaced L$_2$ vertical Lyapunov orbits

Solar sails can be used to create families of displaced libration point orbits in the Earth-Moon system [9, 10]. These orbits can be found by starting from a suitable classical (i.e., no solar-sail acceleration) libration point orbit with a period equal to a fraction or multiple of the Sun's synodic period, see Eq. 11. By subsequently fixing the solar-sail steering law, stepwise increasing the characteristic acceleration of the sail $a_{0,EM}$, and applying a differential correction scheme at each step in $a_{0,EM}$, families of displaced orbits arise. When starting from a classical vertical Lyapunov orbit at L_2 with a period equal to two Sun synodic periods, the family in Fig. 4 is obtained. The adopted steering law is one where the sail tracks the Sun's motion around the Earth-Moon system, but is pitched at an angle of $\alpha = -35.26\,\mathrm{deg}$ with respect to the Earth-Moon orbital plane. This sail orientation creates an out-of-plane acceleration component which displaces the orbits towards the southern hemisphere of the Moon, thereby providing better coverage of the lunar South Pole. If two spacecraft are placed in the orbit for $a_{0,EM} = 0.1$ with a phase difference of half an orbital period, i.e., 29.67 days, those two spacecraft can provide continuous coverage of the Aitken Basin and the lunar South Pole, as well as maintain a direct link with Earth [10]. This constellation is shown in Fig. 5 and these are the two orbits that will be targeted in this paper.

3.2. Earth-centered Highly Elliptical Orbits

The initial parking orbit for the spacecraft is assumed to be a Soyuz highly elliptical orbit [23]. The geometry of the HEO is described using Keplerian elements expressed in an Earth Centered Inertial reference frame, ECI$(\hat{\mathbf{x}}_{ECI}, \hat{\mathbf{y}}_{ECI}, \hat{\mathbf{z}}_{ECI})$ [24, 25]: a perigee altitude of 250 km, an argument of perigee of 178 deg and an inclination of 6 deg. The other Keplerian

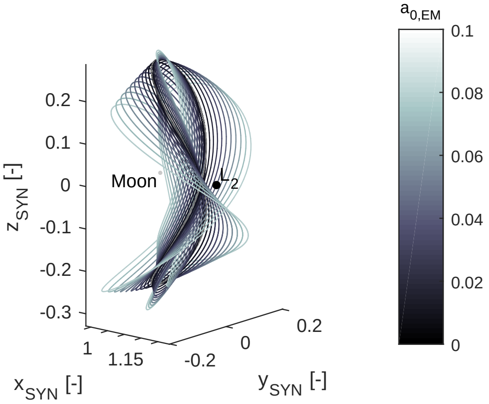

Fig. 4. Families of solar-sail displaced L_2 vertical Lyapunov orbits in the SYN-frame as function of $a_{0,EM}$.

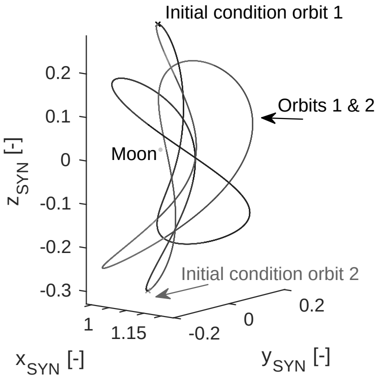

Fig. 5. Constellation of solar-sail displaced L_2 vertical Lyapunov orbits in the SYN-frame.

elements (apogee altitude, right ascension of ascending node, and true anomaly) can be chosen freely. The performance of the Soyuz launch vehicle into a range of HEOs is given in Fig. 6 as a function of the apogee altitude. Note that the ECI-frame is defined as follows: the $\hat{\mathbf{x}}_{ECI}$-axis points towards the vernal equinox, the $\hat{\mathbf{z}}_{ECI}$-axis is oriented perpendicular to the Earth's equatorial plane, and the $\hat{\mathbf{y}}_{ECI}$-axis completes the right-handed reference frame.

3.3. Trajectory design

To design the transfers of the two spacecraft from HEO to the orbits in Fig. 5, the trajectories are split into various segments, see Fig. 7. The initial HEO is described using Keplerian elements, which adheres to two-body (Earth-spacecraft) dynamics. It is assumed that the spacecraft departs from the HEO at GEO altitude, where a switch is made to Earth-Moon three-body dynamics. The first day of the trajectory is modelled as a ballistic segment to allow the sail to deploy. After the first day, when the solar sail is deployed, the main part of the trajectory commences and is propagated until the spacecraft arrives at the solar-sail displaced L_2 vertical Lyapunov orbit (hereafter in short referred to as solar-sail orbit or SSO).

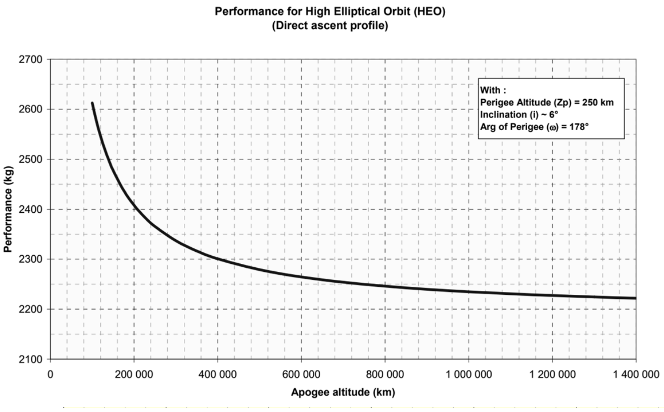

Fig. 6. Transfer mass to HEO as a function of apogee altitude for a Soyuz launch from Guiana Space Centre [23].

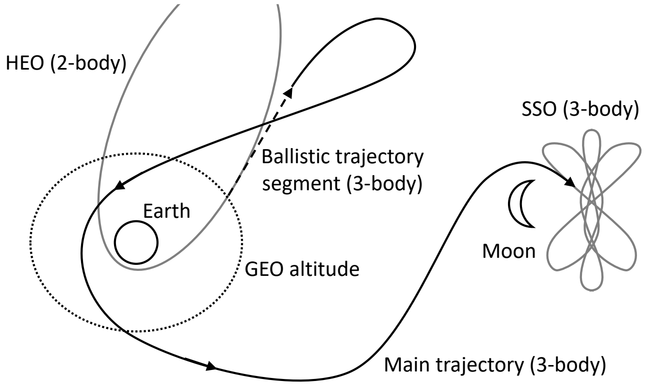

Fig. 7. Schematic of the various trajectory segments.

3.4. Reference frame transformations

In order to constrain the initial state vector of the transfer trajectory to coincide with a HEO, a transformation from the SYN-frame to the ECI-frame and from Cartesian coordinates to Keplerian elements is required. The first step in the transformation from the SYN- to the ECI-frame is to transform the spacecraft's position vector with respect to Earth, $\mathbf{r}_{13}$, to an intermediate reference frame, the ecliptic reference frame, ECL$(\hat{\mathbf{x}}_{ECL}, \hat{\mathbf{y}}_{ECL}, \hat{\mathbf{z}}_{ECL})$. The ECL-frame is an Earth-centered pseudo-inertial right-handed reference frame, where the $\hat{\mathbf{x}}_{ECL}$-axis coincides with the vernal equinox and the $\hat{\mathbf{z}}_{ECL}$-axis is aligned with the angular momentum vector of Earth's orbit around the Sun [24]. The transformation from the SYN-frame to the ECL-frame is given by:

$$[\mathbf{r}_3]_{ECL} = R_3(\Omega_2)R_1(i_2)R_3(\omega_2+\theta_2(t))\mathbf{r}_{13}\cdot U_{length}, \quad (14)$$

and similarly, for the velocity vector $\dot{\mathbf{r}}_3$:

$$[\dot{\mathbf{r}}_3]_{ECL} = R_3(\Omega_2)R_1(i_2)R_3(\omega_2 + \theta_2(t))\cdot \\ (\dot{\mathbf{r}}_3 + \boldsymbol{\omega}_{rot} \times \mathbf{r}_3) \cdot \frac{U_{length}}{U_{time}}, \quad (15)$$

where Ω_2, i_2, ω_2 and θ_2 are the right ascension of the ascending node, inclination, argument of perigee and true anomaly of the Moon with respect to the ECL-frame. Note that the angular progression of the Moon's orbit is equal to the time unit in the CR3BP, i.e., $\theta_2(t) = \theta_{2,0} + t$, where $\theta_{2,0}$ is the true anomaly of the Moon at $t = 0$. The Moon has an inclination of 5.145 deg with respect to the ecliptic. However, during this work it is assumed that the Moon's orbit coincides with the ecliptic plane, resulting in a lunar inclination of 0 deg. For this inclination, Ω_2 and ω_2 are not defined and are thus replaced by a fixed phase angle $\varphi_{2,0} = \Omega_2 + \omega_2 + \theta_{2,0}$. As a result, the rotational matrices in Eq. 14 and 15 can be rewritten as:

$$R_3(\Omega_2)R_1(i_2)R_3(\omega_2 + \theta_2(t)) = R_3(\varphi_{2,0} + t). \quad (16)$$

The state vector expressed in the ECL-frame can then be transformed to the ECI-frame using:

$$[\mathbf{r}_3]_{ECI} = R_1(\delta_{eq})[\mathbf{r}_3]_{ECL}, \quad (17)$$

and

$$[\dot{\mathbf{r}}_3]_{ECI} = R_1(\delta_{eq})[\dot{\mathbf{r}}_3]_{ECL}, \quad (18)$$

where $\delta_{eq} = 23.44$ deg is the obliquity of Earth's rotation axis [20]. The Cartesian state vector $\left[[\mathbf{r}_3]_{ECI}^T \quad [\dot{\mathbf{r}}_3]_{ECI}^T\right]^T$ can then be transformed to Keplerian elements, which should match those of a HEO.

4. INITIAL GUESS GENERATION

Due to the chaotic nature of the CR3BP, it is challenging to find trajectories that depart from a HEO and perfectly arrive at the targeted SSO by just varying the conditions of the departure point along the HEO and assuming a particular steering law. Therefore, instead, as an initial guess for the transfer, a backwards approach is adopted where several state vectors along the SSO are selected from where the dynamics are propagated backwards in time. The integration is terminated if a set altitude above Earth is reached. Along this trajectory a locally optimal steering law (LOSL) is used to determine the sail attitude that maximizes the spacecraft kinetic energy. The LOSL determines this optimal sail attitude by maximizing the solar-sail acceleration along the velocity vector $\left[\dot{\mathbf{r}}_3\right]_{SSF}$ at every integration step along the trajectory. A complete derivation of the LOSL can be found in Ref. [4]. Here, only the result is presented. To compute the optimal attitude, first the spacecraft velocity vector is transformed from the SYN-frame to the SSF-frame, using:

$$[\dot{\mathbf{r}}_3]_{SSF} = \begin{bmatrix} \hat{\mathbf{r}}_{43} \\ \hat{\boldsymbol{\theta}}_{43} \\ \hat{\boldsymbol{\varphi}}_{43} \end{bmatrix} (\dot{\mathbf{r}}_3 + \boldsymbol{\omega}_{rot} \times \mathbf{r}_3). \quad (19)$$

This equation computes the inertial velocity, projected in the SSF-frame. Secondly, the parameter ζ is calculated as a function of the velocity components

$$[\dot{\mathbf{r}}_3]_{SSF} = [v_{x,SSF} \quad v_{y,SSF} \quad v_{z,SSF}] \quad (20)$$

$$\zeta = \frac{-3v_{x,SSF}v_{y,SSF} \pm v_{y,SSF}\sqrt{\xi}}{4(v_{y,SSF}^2 + v_{z,SSF}^2)}, \quad (21)$$

with

$$\xi = 9v_{x,SSF}^2 + 8(v_{y,SSF}^2 + v_{z,SSF}^2) \quad (22)$$

Equation 21 results in two values for ζ due to the $\pm$ sign. Both values of ζ are used to evaluate the desired sail orientation, $\hat{\mathbf{n}}_{SSF} = \left[n_{x,SSF} \quad n_{y,SSF} \quad n_{z,SSF}\right]$, using:

$$n_{x,SSF} = \frac{|v_{y,SSF}|}{\sqrt{v_{y,SSF}^2 + \zeta^2(v_{y,SSF}^2 + v_{z,SSF}^2)}}, \quad (23)$$

$$n_{y,SSF} = \zeta n_{x,SSF} \quad (24)$$

and

$$n_{z,SSF} = \frac{v_{z,SSF}}{v_{y,SSF}} n_{y,SSF}. \quad (25)$$

From the two solutions found, the attitude is selected which maximizes the acceleration along the velocity vector:

$$\mathbf{a}^T[\dot{\mathbf{r}}_3]_{SSF} = a_{0,EM} n_{x,SSF}^2 (\hat{\mathbf{n}}_{SSF} \cdot [\dot{\mathbf{r}}_3]_{SSF}). \quad (26)$$

The LOSL allows for a larger SRP acceleration along the velocity direction than other steering laws, such as the velocity tangent steering law or the on-off switching law also described by Ref [4]. The LOSL can generate small accelerations along the velocity direction, even if the spacecraft is moving towards the Sun.

5. TRAJECTORY TRANSCRIPTION

The trajectories found through the application of the LOSL adhere to the dynamics, but require rapid solar-sail attitude changes, perform flybys at unfeasible altitudes and do not depart from a Soyuz HEO. In order to increase the feasibility of the found trajectories, additional path and point constraints need to be enforced along the trajectory. However, that problem contains an infinite number of dimensions, since the states and controls are described by continuous functions. To reduce the number of dimensions, this section describes the 12^{th}-order Gauss-Lobatto collocation method, which approximates these continuous functions using 7^{th}-degree piecewise polynomials. The continuous trajectory problem then reduces to finding a finite number of polynomials. A set of defect

Table 3. Position of internal and collocation points along τ [15, 16, 14].

Parameter	Type of point	Value
τ_i	node	0
τ_{i1}	defect	8.48880518607166e-2
τ_{i2}	internal	2.65575603264643e-1
τ_{ic}	defect	5.00000000000000e-1
τ_{i3}	internal	7.34424396735357e-1
τ_{i4}	defect	9.15111948139283e-1
τ_{i+1}	node	1

constraints is enforced over these polynomials such that the dynamics are satisfied. Furthermore, path and point constraints are added, resulting in a collection of constraints as a function of the states and controls. The trajectory problem is thus rewritten as a non-linear programming (NLP) problem, which is consequently solved using the Gauss-Newton algorithm in conjunction with a line search method.

5.1. 12$^{\text{th}}$-order Gauss-Lobatto collocation method

The 12th-order Gauss-Lobatto collocation method is described in detail in Ref. [15] and is applied to a solar-sail trajectory problem in Ref. [14]. Higher-order methods, like the 12th-order Gauss-Lobatto collocation method, provide accurate solutions with fewer variables than lower-order methods, such as trapezoid and Hermite-Simpson methods [26]. Furthermore, the required computation time for higher-order methods is significantly lower than the required computation time for lower-order methods.

The method starts by dividing the trajectory into n nodes, connected by $n-1$ segments as illustrated in Fig. 8(a), where every segment is described by a 7th-degree piecewise polynomial, as shown in Fig. 8(b). The polynomial in Fig. 8(b) can be determined by evaluating both the states and dynamics at the two node points, which would result in a 3rd-degree polynomial. In order to increase the degree and thus accuracy of the interpolating polynomial, two internal points are added, namely $\mathbf{x}_{i2}$ and $\mathbf{x}_{i3}$, which results in a 7th-degree polynomial. In addition, three defect points $\mathbf{x}_{i1}$, $\mathbf{x}_{ic}$ and $\mathbf{x}_{i4}$ are added, that are used to evaluate the dynamics and increase the accuracy of the method to $O(\Delta t^{12})$ [15].

The position of the internal and defect points along the segment are given by the parameter τ:

$$\tau_{ik} = \frac{t_k - t_i}{\Delta t_i}, \tag{27}$$

where Δt_i is the timestep over the i^{th} segment, t_k is the time of the k^{th} internal or defect point along the segment and t_i is the time of the i^{th} node point. Values for τ at the internal and defect points are given in Table 3.

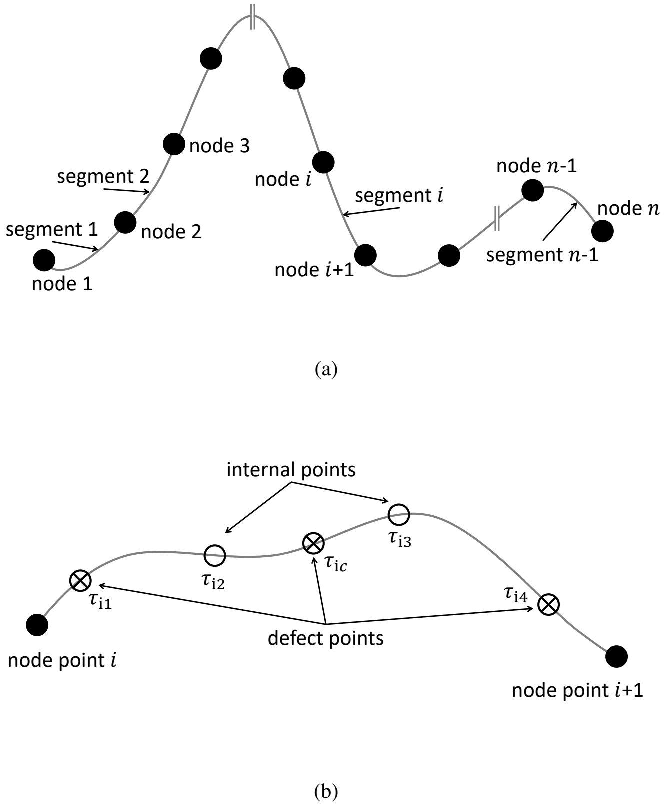

Fig. 8. a) Trajectory divided into nodes and segments. b) Single segment described by a piecewise polynomial as applied in the Gauss-Lobatto method.

The six polynomials representing the six states over a segment are described by:

$$\mathbf{x}_i(\tau) = A_i \begin{bmatrix}1 & \tau & \tau^2 & \tau^3 & \tau^4 & \tau^5 & \tau^6 & \tau^7\end{bmatrix}^T. \tag{28}$$

where the 8 x 6 matrix A_i contains the eight coefficients of each 7th-degree polynomial for the six states on segment i. Matrix A_i can be extracted by matching the polynomial with the states and normalized dynamics at the node and internal points:

$$A_i B = \begin{bmatrix}\mathbf{x}_i & \mathbf{x}'_i & \mathbf{x}_{i2} & \mathbf{x}'_{i2} & \mathbf{x}_{i3} & \mathbf{x}'_{i3} & \mathbf{x}_{i+1} & \mathbf{x}'_{i+1}\end{bmatrix}, \tag{29}$$

where $\mathbf{x}'_{ik} = \Delta t_i \mathbf{f}(t_{ik}, \mathbf{x}_{ik}, \mathbf{u}_{ik})$ and matrix B is given by:

$$B = \begin{bmatrix} 1 & 0 & 1 & 0 & 1 & 0 & 1 & 0 \\ 0 & 1 & \tau_{i2} & 1 & \tau_{i3} & 1 & 1 & 1 \\ 0 & 0 & \tau_{i2}^2 & 2\tau_{i2} & \tau_{i3}^2 & 2\tau_{i3} & 1 & 2 \\ 0 & 0 & \tau_{i2}^3 & 3\tau_{i2}^2 & \tau_{i3}^3 & 3\tau_{i3}^2 & 1 & 3 \\ 0 & 0 & \tau_{i2}^4 & 4\tau_{i2}^3 & \tau_{i3}^4 & 4\tau_{i3}^3 & 1 & 4 \\ 0 & 0 & \tau_{i2}^5 & 5\tau_{i2}^4 & \tau_{i3}^5 & 5\tau_{i3}^4 & 1 & 5 \\ 0 & 0 & \tau_{i2}^6 & 6\tau_{i2}^5 & \tau_{i3}^6 & 6\tau_{i3}^5 & 1 & 6 \\ 0 & 0 & \tau_{i2}^7 & 7\tau_{i2}^6 & \tau_{i3}^7 & 7\tau_{i3}^6 & 1 & 7 \end{bmatrix}. \tag{30}$$

If matrix A_i is known, the states can be interpolated at any given point on the i^{th} segment using Eq. 28. The control defines the sail normal direction $\hat{\mathbf{n}}_{SSF}(t)$ over each segment through the variables $\mathbf{u}_i$ and $\dot{\mathbf{u}}_i$, and is modelled to vary semi-linearly over each segment and such that $|\hat{\mathbf{n}}_{SSF}(t)| = 1$:

$$\hat{\mathbf{n}}_{SSF}(t) = \mathbf{u}(t) = \frac{\mathbf{u}_i + (t - t_i)\dot{\mathbf{u}}_i}{|\mathbf{u}_i + (t - t_i)\dot{\mathbf{u}}_i|}. \qquad (31)$$

5.2. Defect constraints

Although the polynomial in Fig. 8(b) describes the states over a segment, it does not automatically satisfy the dynamics. Therefore, at the three defect points $\mathbf{x}_{i1}$, $\mathbf{x}_{ic}$ and $\mathbf{x}_{i4}$, the defect constraints are evaluated, forcing the polynomial to adhere to the dynamics. The defect constraints can be illustrated using Fig. 9.

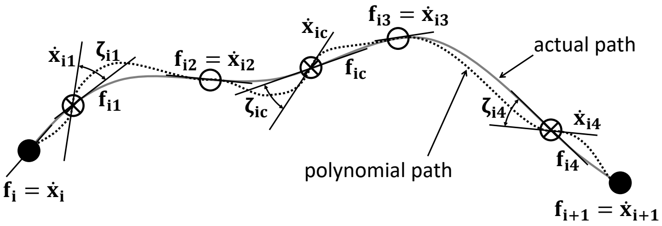

Fig. 9. Sketch containing a visualization of the defect constraints $\boldsymbol{\zeta}_i$. Adapted from Ref. [14].

The states at the defect points are found using [15]:

$$\begin{aligned}\mathbf{x}_{i1} = {} & a_{i1}\mathbf{x}_i + a_{i21}\mathbf{x}_{i2} + a_{i31}\mathbf{x}_{i3} + a_{ip1}\mathbf{x}_{i+1} + \\ & \Delta t_i \left(v_{i1}\mathbf{f}_i + v_{i21}\mathbf{f}_{i2} + v_{i31}\mathbf{f}_{i3} + v_{ip1}\mathbf{f}_{i+1} \right),\end{aligned} \qquad (32)$$

$$\begin{aligned}\mathbf{x}_{ic} = {} & a_{ic}\mathbf{x}_i + a_{i2c}\mathbf{x}_{i2} + a_{i3c}\mathbf{x}_{i3} + a_{ipc}\mathbf{x}_{i+1} + \\ & \Delta t_i \left(v_{ic}\mathbf{f}_i + v_{i2c}\mathbf{f}_{i2} + v_{i3c}\mathbf{f}_{i3} + v_{ipc}\mathbf{f}_{i+1} \right),\end{aligned} \qquad (33)$$

and

$$\begin{aligned}\mathbf{x}_{i4} = {} & a_{i4}\mathbf{x}_i + a_{i24}\mathbf{x}_{i2} + a_{i34}\mathbf{x}_{i3} + a_{ip4}\mathbf{x}_{i+1} + \\ & \Delta t_i \left(v_{i4}\mathbf{f}_i + v_{i24}\mathbf{f}_{i2} + v_{i34}\mathbf{f}_{i3} + v_{ip4}\mathbf{f}_{i+1} \right),\end{aligned} \qquad (34)$$

where the required constants a and v are given in Ref. [15, 16]. Using the node, internal and defect points, the defect constraints, $\boldsymbol{\zeta}$, are evaluated as [15]:

$$\begin{aligned}\boldsymbol{\zeta}_{i1} = {} & b_{i1}\mathbf{x}_i + b_{i21}\mathbf{x}_{i2} + b_{i31}\mathbf{x}_{i3} + b_{ip1}\mathbf{x}_{i+1} + \\ & \Delta t_i \left(w_{i1}\mathbf{f}_i + w_{i11}\mathbf{f}_{i1} + w_{i21}\mathbf{f}_{i2} + w_{i31}\mathbf{f}_{i3} + w_{ip1}\mathbf{f}_{i+1} \right),\end{aligned} \qquad (35)$$

$$\begin{aligned}\boldsymbol{\zeta}_{ic} = {} & b_{ic}\mathbf{x}_i + b_{i2c}\mathbf{x}_{i2} + b_{i31}\mathbf{x}_{i3} + b_{ipc}\mathbf{x}_{i+1} + \\ & \Delta t_i \left(w_{ic}\mathbf{f}_i + w_{i2c}\mathbf{f}_{i2} + w_{icc}\mathbf{f}_{ic} + w_{i3c}\mathbf{f}_{i3} + w_{ipc}\mathbf{f}_{i+1} \right),\end{aligned} \qquad (36)$$

and

$$\begin{aligned}\boldsymbol{\zeta}_{i4} = {} & b_{i4}\mathbf{x}_i + b_{i24}\mathbf{x}_{i2} + b_{i34}\mathbf{x}_{i3} + b_{ip4}\mathbf{x}_{i+1} + \\ & \Delta t_i \left(w_{i4}\mathbf{f}_i + w_{i24}\mathbf{f}_{i2} + w_{i34}\mathbf{f}_{i3} + w_{i44}\mathbf{f}_{i4} + w_{ip4}\mathbf{f}_{i+1} \right),\end{aligned} \qquad (37)$$

where the constants b and w are also given in Ref. [15, 16]. If the value of $\boldsymbol{\zeta}$ is equal to zero, the dynamics over the polynomial are accurately approximated up to $O(\Delta t_i^{12})$ [14].

5.3. Path constraints

The defect constraints are used to comply with the dynamics of the system. For a feasible trajectory, it is also required to comply with a set of path (in)equality constraints, $\mathbf{g}$. As inequality constraints cannot be solved directly by NLP solvers [17], they are rewritten to introduce slack variables, transforming the inequality constraints in equality constraints [14]. The introduction of slack variables enables the inequality constraint to be active at every node point. Although this requires the algorithm to always evaluate every constraint, it eliminates the need for determining the active-set of constraints.

5.3.1. Path constraints on the control vector

The control, $\mathbf{u}(t) = \hat{\mathbf{n}}_{SSF}(t)$ is described by a Cartesian unit vector. As the sail normal vector cannot have a component in the direction of the Sun, i.e., the cone angle can only take on values between 0 and 90 deg, the $u_{x,SSF,i}$ element needs to be constrained to be larger than zero. This is ensured through the implementation of the following path constraint:

$$g_{i1} = u_{x,SSF,i} - \eta_{i1}^2. \qquad (38)$$

The corresponding slack variable η_{i1} should thus equal $\sqrt{u_{x,SSF,i}}$. If $u_{x,SSF,i}$ becomes smaller than zero, the constraint in Eq. 38 will always be violated for any real η_{i1}, and thus the constraint ensures $u_{x,SSF,i} \geq 0$.

As the control describes a unit vector, it is also required for the norm of the control to be equal to 1, i.e., $|\mathbf{u}_i| = 1$, which can be expressed as a path constraint as:

$$g_{i2} = 1 - \sqrt{u_{x,SSF,i}^2 + u_{y,SSF,i}^2 + u_{z,SSF,i}^2}. \qquad (39)$$

Finally, three control continuity constraints across the segments are included, which ensure that the control over the trajectory is described by a piecewise linear function:

$$g_{i3} = u_{x,SSF,i} + \dot{u}_{x,SSF,i}\Delta t_i - u_{x,SSF,i+1}, \qquad (40)$$

$$g_{i4} = u_{y,SSF,i} + \dot{u}_{y,SSF,i}\Delta t_i - u_{y,SSF,i+1} \qquad (41)$$

and

$$g_{i5} = u_{z,SSF,i} + \dot{u}_{z,SSF,i}\Delta t_i - u_{z,SSF,i+1}. \qquad (42)$$

5.3.2. Path constraints on the trajectory altitude

In order to avoid impact and numerical integration issues during flybys, altitude constraints are introduced. First of all, a minimum altitude with respect to Earth is enforced of $h_{31,min}$ = 3,000 km. Similarly, the minimum altitude with respect to the Moon is set equal to four Moon radii or $h_{32,min}$ = 6,952 km. The minimum altitude constraints are scaled to dimensionless units and rewritten to equality constraints through the slack variables η_{i2} and η_{i3} resulting in:

$$g_{i6} = R_e + h_{31,min} - r_{31,i} + \eta_{i2}^2, \tag{43}$$

and

$$g_{i7} = R_m + h_{32,min} - r_{32,i} + \eta_{i3}^2. \tag{44}$$

where R_e and R_m are the body radii of the Earth and Moon, respectively, and r_{i31} and r_{i32} are the distances between the spacecraft and the Earth and Moon, respectively, at the i^{th} node.

5.3.3. Path constraint on sail rotation rate

A solar sail is a flexible structure with a large moment of inertia. Rapid changes in attitude are therefore not feasible for large sails. The maximum rotation rate of the solar sail with respect to the Sun-sail line will therefore be constrained to $\dot{u}_{max}$ = 20 deg/day. If $\Delta\phi_i$ is a rotation of the solar sail over segment i, it can be assumed that $\Delta\phi_i/\Delta t_i \approx |\dot{\mathbf{u}}|$ for small Δt_i. After converting the 20 deg/day to dimensionless units, the rotation rate constraint is enforced in the form:

$$\begin{aligned} g_{i8} = 0.01(\dot{u}_{max} - \\ \sqrt{\dot{u}_{x,SSF,i}^2 + \dot{u}_{y,SSF,i}^2 + \dot{u}_{z,SSF,i}^2} - \eta_{i4}^2), \end{aligned} \tag{45}$$

where the constraint is scaled by a factor 0.01 to improve convergence of the NLP-solver.

As can be seen from Eqs. 38-45, a total of eight path constraints are active at each node point.

5.4. Point constraints

The defect and path constraints allow for the construction of dynamically feasible trajectories. In order to also depart from a HEO and arrive at the SSO, further point constraints are enforced. First, nine point constraints are added on the final node to ensure that the final states and controls comply with the SSO:

$$\mathbf{c}_n = \begin{bmatrix} \mathbf{x}_n \\ \mathbf{u}_n \end{bmatrix} - \begin{bmatrix} \mathbf{x}_{SSO}(t_n) \\ \mathbf{u}_{SSO}(t_n) \end{bmatrix}. \tag{46}$$

In addition, three point constraints are added on the departure node, such that the trajectory departs from GEO-altitude, r_{GEO} = 35,786 km, and from an orbit orientation that coincides with a Soyuz HEO:

$$\mathbf{c}_1 = \begin{bmatrix} |\mathbf{r}_{13}| \\ i_{ECI} \\ \omega_{ECI} \end{bmatrix} - \begin{bmatrix} r_{GEO}/U_{length} \\ i_{HEO} \\ \omega_{HEO} \end{bmatrix}, \tag{47}$$

where i_{ECI} and ω_{ECI} are obtained from the transformation in Section 3.4 and i_{HEO} and ω_{HEO} are the inclination and argument of perigee of a Soyuz HEO.

5.5. The Gauss-Newton algorithm

In order to solve the trajectory problem, the states and constraints are rewritten as an NLP problem. Let the decision variables for a single segment be collected in a decision vector $\mathbf{X}_i$ of size 28 x 1:

$$\mathbf{X}_i = \begin{bmatrix} \mathbf{x}_i^T & \mathbf{u}_i^T & \dot{\mathbf{u}}_i^T & \mathbf{x}_{i,2}^T & \mathbf{x}_{i,3}^T & \boldsymbol{\eta}_i^T \end{bmatrix}^T, \tag{48}$$

subjected to the 26 x 1 constraint vector:

$$\mathbf{F}_i = \begin{bmatrix} \boldsymbol{\zeta}_{i1}^T & \boldsymbol{\zeta}_{ic}^T & \boldsymbol{\zeta}_{i4}^T & \mathbf{g}_i^T \end{bmatrix}^T. \tag{49}$$

For all segments, the decision vector becomes:

$$\mathbf{X} = \begin{bmatrix} \mathbf{X}_1^T & \mathbf{X}_2^T & \dots & \mathbf{X}_{n-2}^T & \mathbf{X}_{n-1}^T & \mathbf{x}_n^T & \mathbf{u}_n^T \end{bmatrix}^T, \tag{50}$$

with the corresponding constraint vector:

$$\mathbf{F} = \begin{bmatrix} \mathbf{c}_1^T & \mathbf{F}_1^T & \mathbf{F}_2^T & \dots & \mathbf{F}_{n-2}^T & \mathbf{F}_{n-1}^T & \mathbf{c}_n^T \end{bmatrix}^T. \tag{51}$$

For a trajectory consisting of n segments, a total of $28(n-1)+9$ decision variables are used to satisfy $26(n-1)+12$ constraints. For a trajectory of 50 nodes, this would result in 1381 variables subject to 1286 constraints, which would be excessively large to solve using grid searches, Monte-Carlo methods or genetic algorithms. Since all constraints are smooth and differentiable, the Gauss-Newton algorithm is used to find the decision vector $\mathbf{X}$ for which $\mathbf{F} = \mathbf{0}$ [14]. The Gauss-Newton algorithm minimizes the sum of the squared constraint violations, converges quadratically [19] and does not require the computation of second order derivatives. Although there are an infinite number of search directions $D\mathbf{X}$ which satisfy:

$$\mathbf{F}(\mathbf{X}) = \frac{\partial \mathbf{F}(\mathbf{X})}{\partial \mathbf{X}} \cdot D\mathbf{X}, \tag{52}$$

the Gauss-Newton algorithm solves for the minimum norm value of $D\mathbf{X}$, such that the characteristics of the initial guess are best preserved [19]. Since the initial guess is a locally optimal solution with respect to increasing the spacecraft's energy, it is indeed desired to find a feasible trajectory close to the initial guess.

First, the derivative of the constraint vector $\mathbf{F}$ with respect to $\mathbf{X}$ is calculated, resulting in the Jacobi matrix ($D\mathbf{F} = \frac{\partial \mathbf{F}(\mathbf{X})}{\partial \mathbf{X}}$). Note that $\mathbf{F}_i$ is only dependent on $\mathbf{X}_i$, $\mathbf{x}_{i+1}$ and $\mathbf{u}_{i+1}$. Similarly, the point constraints $\mathbf{c}_1$ and $\mathbf{c}_n$ are only dependent on the departure and arrival node. In order to calculate $D\mathbf{F}$ efficiently, only the relevant derivatives have to be evaluated, while the other derivatives are known a priori to be equal to zero.

The efficient calculation of the derivatives is achieved by using the complex step method, which gives an accuracy similar to that of the central step method, with only a single function evaluation [27]. The j^{th} column of $D\mathbf{F}_i$ can be calculated by adding a small imaginary number to the j^{th} element of vector $\mathbf{X}_i$ and evaluating $\mathbf{F}_i$ using the complex step method:

$$\frac{\partial \mathbf{F}_i}{\partial X_{ij}} = \frac{1}{\epsilon} Imag(\mathbf{F}_i([X_{i1} \quad \dots \quad X_{i(j-1)} \quad X_{ij} + \epsilon\sqrt{-1} \quad X_{i(j+1)} \quad \dots \quad X_{i28} \quad \mathbf{x}_{i+1}^T \quad \mathbf{u}_{i+1}^T])), \tag{53}$$

where the partial Jacobi matrix $\frac{\partial \mathbf{F}_i}{\partial \mathbf{X}_i}$ has size 26 x 19 and ϵ is a small constant of value 10^{-10}. Note that the partial derivatives $\frac{\partial \mathbf{F}_i}{\partial \mathbf{x}_{i+1}}$, $\frac{\partial \mathbf{F}_i}{\partial \mathbf{u}_{i+1}}$, $\frac{\partial \mathbf{c}_1}{\partial \mathbf{X}_1}$, $\frac{\partial \mathbf{c}_n}{\partial \mathbf{x}_n}$ and $\frac{\partial \mathbf{c}_n}{\partial \mathbf{u}_n}$ also need to be evaluated. The structure containing the non-zero elements of the complete Jacobi matrix using seven nodes is shown in Fig. 10.

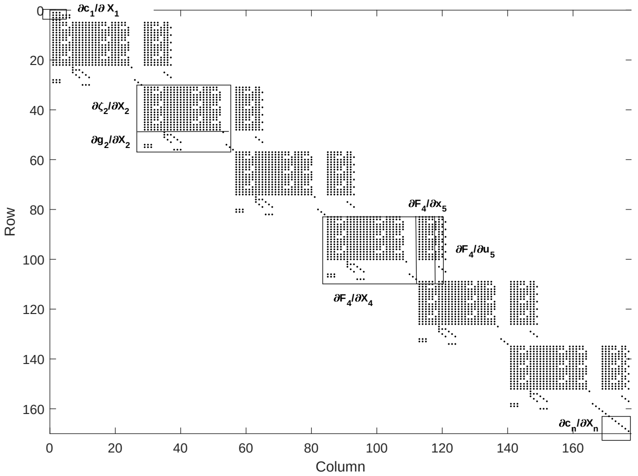

Fig. 10. Structure of nonzero elements of the Jacobi matrix ($D\mathbf{F}$) for a trajectory problem with six segments and seven nodes.

The Jacobi matrix is applied in the Gauss-Newton algorithm to determine the search direction $D\mathbf{X}$ [14]:

$$D\mathbf{X} = -D\mathbf{F}(\mathbf{X}) \left(\left[D\mathbf{F}(\mathbf{X}) \cdot D\mathbf{F}(\mathbf{X})^T \right]^{-1} \mathbf{F}(\mathbf{X}) \right). \tag{54}$$

Note that if $n = 50$, the matrix $D\mathbf{F}$ has dimensions 1234 x 1381, containing just 26,959 (1.582%) non-zero elements, which can be efficiently stored using MATLAB®'s *sparse.m* function. Furthermore, the matrix multiplications and inverses of $D\mathbf{F}$ are efficiently calculated using the unsymmetric multifrontal method provided by UMFPACK [28].

The found search direction varies in quality due to nonlinear changes in the dynamics or constraints, especially if the initial guess is far away from a solution or if close flybys around the Earth or Moon are present. In order to improve the radius of convergence, a line search algorithm is used in the form [17]:

$$\mathbf{X}_{new} = \mathbf{X} + \alpha_{ls} D\mathbf{X}, \tag{55}$$

where α_{ls} is a parameter with a value selected between 0.1 and 1.0 that minimizes $\sum \mathbf{F}(\mathbf{X}+\alpha_{ls}D\mathbf{X})$. If the search direction points in an unfeasible direction, the linesearch algorithm multiplies the search direction with a small number, resulting in a new estimate of $\mathbf{X}_{new}$. From this new point, a new and potentially better search direction can be found. This procedure is repeated untill all constraints are met up to $O(10^{-10})$.

6. MESH AND ERROR CONTROL

Although the 12th-order Gauss-Lobatto method is highly accurate, a discretization error is made across every segment, which can become unbounded during close approaches of the Earth or Moon. In order to decrease the discretization error over the trajectory, the number of linearly spaced nodes can be increased, but this would increase the computation time. A more efficient method is to estimate the error made over each segment and adjust the mesh spacing accordingly. An optimal mesh distributes the nodes such that the error over each segment is constant. The piecewise polynomials have degree seven, for which the error over the i^{th} segment can be approximated using:

$$e_i = C\Delta t_i^8 ||\mathbf{x}_i^{(8)}|| + O(\Delta t_i^9) \tag{56}$$

where C is a dimensionless constant equal to approximately $2.935793951 \times 10^{-9}$ [29] and $\mathbf{x}^{(8)}$ is the 8^{th}-order derivative of the state vector. Since $\mathbf{x}$ is described by a 7^{th}-degree polynomial, see Eq. 28, the 8^{th}-order derivative is unknown. However, it can be approximated by applying a difference formula in order to evaluate $\mathbf{x}^{(8)}$ over multiple segments [18]:

$$||\mathbf{x}^{(8)}|| \approx \max \left[2\frac{|\mathbf{y}_1 - \mathbf{y}_2|}{\Delta t_1 + \Delta t_2} \right] \text{ over } (t_1, t_2) \tag{57}$$

$$||\mathbf{x}^{(8)}|| \approx \max \left[\frac{|\mathbf{y}_{i-1} - \mathbf{y}_i|}{\Delta t_{i-1} + \Delta t_i} + \frac{|\mathbf{y}_{i+1} - \mathbf{y}_{i+2}|}{\Delta t_{i+1} + \Delta t_{i+2}} \right] \text{ over } (t_i, t_{i+1}) \tag{58}$$

$$||\mathbf{x}^{(8)}|| \approx \max \left[2\frac{|\mathbf{y}_{n-2} - \mathbf{y}_{n-1}|}{\Delta t_{n-2} + \Delta t_{n-1}} \right] \text{ over } (t_{n-2}, t_{n-1}) \tag{59}$$

where $\mathbf{y}_i$ is the dimensionless 7^{th} order derivative on segment i, given by:

$$\mathbf{y}_i = \frac{\mathbf{x}^{(7)}(\tau)}{\Delta t_i} = 7![\mathbf{x}_i \quad \mathbf{x}_i' \quad \mathbf{x}_{i2} \quad \mathbf{x}_{i2}' \quad \mathbf{x}_{i3} \quad \mathbf{x}_{i3}' \mathbf{x}_{i+1} \quad \mathbf{x}_{i+1}'] \cdot \frac{\mathbf{b}}{\Delta t_i^7}, \tag{60}$$

in which $\mathbf{b}$ is the last column of B^{-1}. The new node points can now be computed using [14]:

$$t_{i+1} = I(t_{i+1})^{-1} \left[\frac{iI(t_n)}{n-1} \right] \tag{61}$$

where

$$I(t) = \int_{t_1}^{t} \theta_8(s)^{1/8} ds. \tag{62}$$

Since the approximation is a piecewise constant function, the integral $I(t)$ is a piecewise linear function, which can be solved for t_{i+1} in Eq. 61. Using the new mesh, the states are interpolated using Eq. 28, such that the dynamics are conserved. Similarly, the control and control derivative are also interpolated. Finally, the slack variables, $\boldsymbol{\eta}$, are recalculated for the new controls and states, such that the path constraint violation of the new mesh is minimized.

Note that the activation of the solar sail after the one-day ballistic phase generates a discontinuity in the dynamics. Therefore, the trajectory before activation and the trajectory after activation of the solar sail are treated as different phases in the error estimation algorithm. As a result, the moment at which the solar sail is activated, always coincides with a node point.

7. DESIGN PROCESS

In order to generate feasible transfer trajectories, the theory described in the previous sections is applied in a systematical manner. First, an initial guess to the trajectory optimization problem is generated. Secondly, the departure altitude as well as the perigee altitude of the HEO orbit are reduced using a stepwise approach. If a transfer trajectory with a perigee altitude of 250 km is found, the parking orbit inclination and argument of perigee constraints are enforced. Once one trajectory is found, a novel method to obtain the trajectory for the second spacecraft in the constellation is applied and a mass budget analysis is conducted to obtain achievable spacecraft (payload) masses.

7.1. Generating the initial guess

To generate an initial guess for the trajectory, first a fixed arrival time, $t_{arrival}$, on the SSO is selected. To find the corresponding state, $\mathbf{x}_{SSO}$, the states are integrated along the SSO from $t = 0$ to $t_{arrival}$ using MATLAB®'s *ode45.m* function [30] in accordance with Section 3.1. An initial guess for the transfer trajectory is subsequently generated by propagating the dynamics of the CR3BP from $\mathbf{x}_{SSO}$ in reverse time, where the LOSL is used to determine the control along the trajectory. The backwards propagated trajectory is truncated at the point with the closest approach to GEO-altitude within a maximum allowable transfer time. The trajectory is rewritten as the NLP problem described in Section 5, by evaluating the states, controls, rotation rates and slack variables on the node and internal points. In total, 100 equally spaced node points per lunar period are used to describe the initial guess.

7.2. Enforcing altitude constraints

In order to increase the feasibility of the trajectory, constraints are enforced through the collocation method. In addition to the constraints, the sail acceleration is set to zero during the first day of the trajectory, allowing enough time for the solar sail to deploy. The altitude constraint on the departure point is gradually introduced, reducing the altitude of the departure point to GEO-altitude using ten consecutive steps. During each step, the constraints in the NLP problem are enforced using the Gauss-Newton algorithm, followed by a new mesh refinement with an equidistributed error. Such a stepwise approach is applied as the initial guess may be far from a constraint-satisfying solution and the NLP-solver might diverge for such large constraint violations. Furthermore, intermediate mesh refinements will improve the convergence to a feasible solution. When the departure point coincides with GEO-altitude, the orbital elements of the parking orbit corresponding to the departure point are calculated. The GEO-altitude constraint is then replaced by the perigee altitude constraint and is reduced in a similar stepwise approach to 250 km using 20 steps. During the perigee reduction steps, no altitude constraint on the departure point is enforced. The altitude of the departure point might therefore depart from GEO-altitude and thus, the trajectory is trimmed by cutting or propagating the starting point at/up to GEO-altitude. This allows for small variations in the overall transfer time during each iteration and enables a wider radius of convergence.

7.3. Enforcing HEO constraints

If a trajectory is found with a perigee altitude of 250 km and a departure altitude equal to GEO altitude, additional constraints are enforced such that the trajectory coincides with a HEO of the Soyuz launcher described in Section 3.2. An inclination constraint of 6 deg as well as an argument of perigee constraint of 178 deg are enforced in a single step. Note that, in order to complete the transformation between the ECL- and SYN-frames, a phase angle $\varphi_{2,0}$ in Eq. 16 is selected through a grid search, for which the discrepancy with respect to the newly enforced constraints is minimal.

7.4. Trajectory for spacecraft 2

Once one feasible trajectory (for the first spacecraft in the constellation) is found, a second trajectory is sought for spacecraft 2. Preferably, both spacecraft are launched at the same time with the same launcher, reducing mission cost and complexity, and providing immediate access to the full constellation. This requires two distinct transfer trajectories with different arrival points along the SSO, but with identical departure conditions. It is difficult to exactly match six states at a set departure time, even using the collocation method described in this work. Therefore the following method is adapted. From initial results, it appeared that the transfer trajectories and departure conditions remain close to the Earth-Moon orbital plane. In addition, the targeted SSO is close to symmetrical in the $(\hat{\mathbf{x}}_{SYN}, \hat{\mathbf{y}}_{SYN})$-plane (the out-of-plane acceleration component used to produce the displaced vertical Lyapunov orbits causes the orbit to be slightly non-symmetric). Still, the found trajectory for spacecraft 1 can be mirrored in the $(\hat{\mathbf{x}}_{SYN}, \hat{\mathbf{y}}_{SYN})$-plane for use as initial guess for spacecraft 2. This results in a trajectory that satisfies the dynamics and path constraints, but with minor constraint violations on the departure point and major constraint violations on the arrival point. Furthermore, since the entire trajectory is mirrored, the out-of-plane control component, $n_{z,SSF}$, upon arrival is pitched in the opposite direction with respect to the desired SSO attitude. Finally, because the SSO is not perfectly symmetric in the $(\hat{\mathbf{x}}_{SYN}, \hat{\mathbf{y}}_{SYN})$-plane, this causes a small offset between the final node and the SSO. In order to reduce these constraint violations, an additional trajectory phase is added at the end of the transfer to allow the control to reverse its $n_{z,SSF}$-component. As an initial guess for this phase, the states of the SSO are used over which the control varies semi-linear from $\hat{\mathbf{n}}_{SSF,SC2}(t_{f,SC1}) = \begin{bmatrix}\cos\alpha & 0 & \sin\alpha\end{bmatrix}^T$ to $\hat{\mathbf{n}}_{SSF,SC2}(t_{f,SC2}) = \begin{bmatrix}\cos\alpha & 0 & -\sin\alpha\end{bmatrix}^T$ in accordance with Eq. 31, with $\alpha = 35.26\,\text{deg}$ as in Section 3.1. Note that the subscripts "SC1" and "SC2" refer to spacecraft 1 and 2, respectively. A total of 50 nodes are used to describe this phase, with a time length of π/Ω_s, which equals 14.84 days.

7.5. Spacecraft mass budget

Once the trajectory for both spacecraft 1 and 2 are found, the last step is to conduct a preliminary spacecraft mass budget analysis. Two scenario's are considered. The first scenario considers the mass breakdown for two large satellites, utilizing the complete payload capacity of a single Soyuz launch. The second scenario considers a CubeSat demonstration mission, with assumed spacecraft masses of 10 kg. A parametric mass analysis is carried out to find an estimation of the subsystem masses. As solar-sail technology is relatively new, no reliable mass estimation can be made based on reference satellite data. Instead mass fractions for communication satellites are used from Ref. [31], where the mass fraction used for the propulsion subsystem is replaced by a calculation of the required sail area and consequently the required sail mass. The used mass fractions are shown in Table 4.

Table 4. Mass fractions for communication satellites from Ref. [31]. Normalized mass fractions found by removing the propulsion subsystem.

	Fractions	Normalized fractions
Payload	0.274	0.2857
Structure	0.213	0.221
Thermal	0.036	0.0375
Power	0.319	0.3326
TT&C	0.048	0.0501
ADCS	0.069	0.0719
Propulsion	0.038	-

The solar-sail mass can be calculated as a function of the solar-sail area, A_s, using the critical sail loading, σ^*, of 1.53 g/m^2 [4] and the lightness number β_0:

$$\beta_0 = \sigma^* \frac{A_s}{m_3} = \frac{a_{0,EM} r_S^2}{\mu_4}, \tag{63}$$

where r_S is the distance to the Sun equal to 149.6 x 10^6 km [20] and μ_4 is the gravitational parameter of the Sun equal to 1.32712 x 10^6 km^3/s^2 [20]. Using these values and a dimensional $a_{0,EM}$ of 0.2698 mm/s^2 (corresponding to a dimensionless value of 0.1), it is found that β_0 equals 0.0455. The spacecraft mass, m_3, is extracted from Fig. 6 and is used to determine the required sail area. The solar-sail mass can then be calculated using:

$$m_s = A_s \sigma_s \tag{64}$$

where the sail loading σ_s is assumed equal to 0.010 kg/m^2, which is considered feasible for near-term sail technology [32].

8. INITIAL GUESSES

This section presents the results of the first step in the approach outlined in Section 7: the trajectories created with the LOSL. In order to generate a complete map of possible initial guess transfers, 2000 trajectories are generated by varying the arrival location along the SSO. For a propagation time of 365 days, the results in Fig. 11 are obtained. In Fig. 11, the distance with respect to Earth over time of these trajectories is shown as a function of the arrival time on the SSO (2000 sample points). This arrival time, t_{arr}, is expressed as a fraction of the orbital period, P_{SSO}. Note that an arrival time of $t_{arr} = 0$ corresponds to the most northerly point of the vertical Lyapunov orbit.

The actual distance with respect to Earth is provided by the grayscale in Fig. 11. Due to the reverse time propagation, the spacecraft starts at a large distance (light colour) at zero-transfer time. Over the reverse time propagation (along the horizontal axis), the trajectory will generally start to decrease its distance with respect to Earth, which is shown by the darker shaded areas. The propagation is terminated when the distance becomes less than 250 km or if the distance reaches two Earth-Moon distances or if the solar sail crashes into the Moon.

From Fig. 11 it is clear that most arrival conditions enable transfers that get close to Earth, where the long section

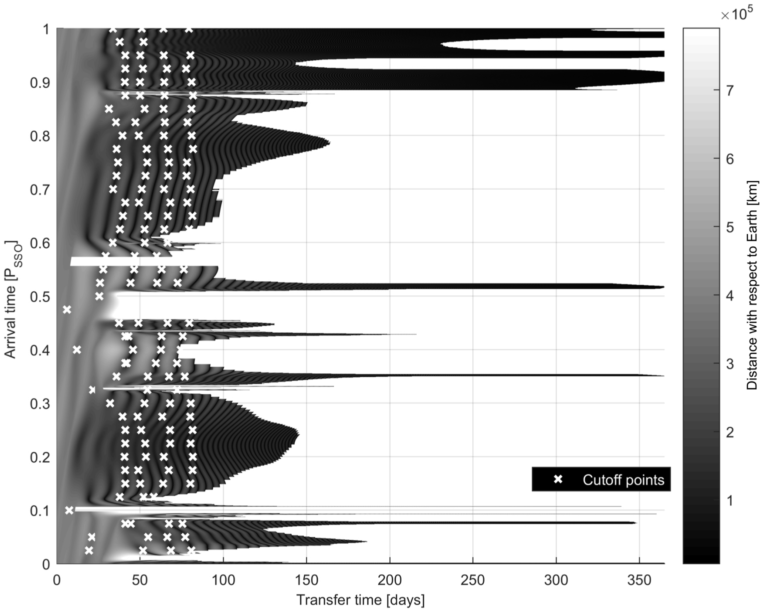

Fig. 11. Earth-spacecraft distance as a function of the arrival time on the SSO and transfer time to the SSO, including the cutoff points for the initial guesses of the collocation method.

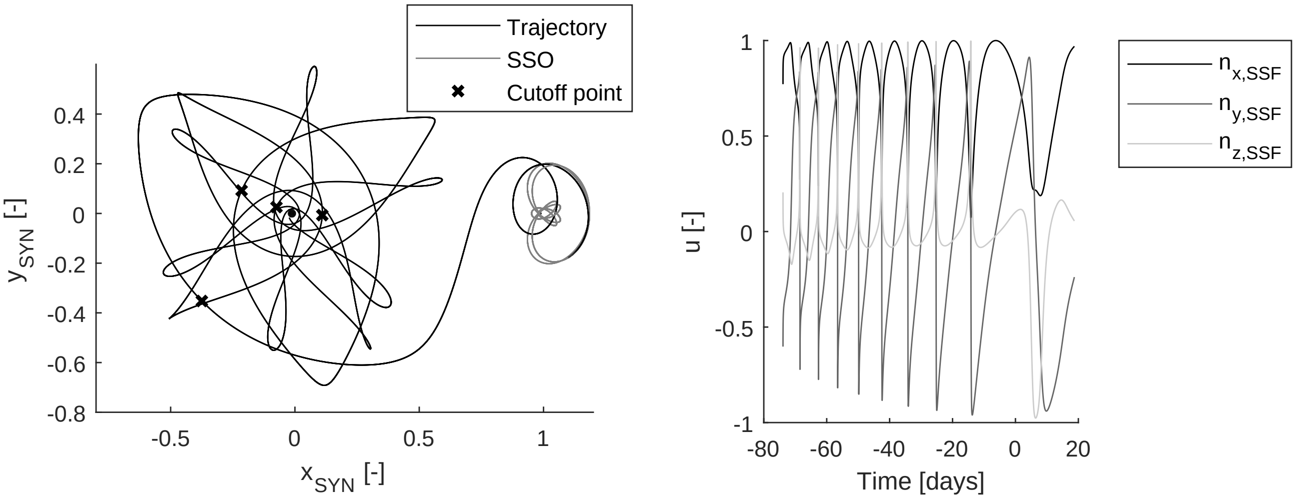

(a)

(b)

Fig. 12. a) Transfer trajectory using locally optimal steering law for an arrival time of $t_{arr} = 1.4\pi/\Omega_s = 0.35P_{SSO}$. b) Corresponding sail attitude.

of dark colors along the horizontal direction indicate that the spacecraft enters a spiral trajectory around Earth until an altitude of 250 km is reached. The geometry of the trajectory varies significantly by changing the arrival location along the SSO. For example, the quickest trajectory that reaches an altitude of 250 km departs at $t_{arr} = 0.1205P_{SSO}$ and achieves a transfer time of 50.7 days. Alternatively, if an arrival time in the range of $t_{arr} = 0.890P_{SSO}$ to $t_{arr} = 1P_{SSO}$ is selected, trajectories are found containing a lengthy Earth-bound spiral connected to a parking orbit similar to a geostationary transfer orbit. Instead, a trajectory that arrives between $t_{arr} = 0.456P_{SSO}$ and $t_{arr} = 0.507P_{SSO}$ travels past the L_2 point and escapes the Earth-Moon system, while a trajectory arriving between $t_{arr} = 0.556P_{SSO}$ and $t_{arr} = 0.573P_{SSO}$ crashes into the Moon. An example trajectory for $t_{arr} = 0.35P_{SSO}$ is shown in Fig. 12(a), with the corresponding solar-sail control in Fig. 12(b). It can be seen that, forwards in time, this trajectory departs from a highly elliptic orbit around Earth and performs multiple flybys close to the Earth. After a total transfer time of 108.88 days, the spacecraft arrives at the SSO. Note that the rapid changes in the Cartesian components of the control in Fig. 12(b) require an extremely agile solar sail.

9. RESULTS

9.1. Inactive rotation rate constraint

While the LOSL transfers that are truncated at an Earth altitude of 250 km match the required perigee altitude of the Soyuz parking orbits, the required inclination and argument of perigee of the HEO are unaccounted for. Furthermore, the lengthy Earth-bound spirals contain multiple flybys at altitudes lower than 1,000 km, which is not considered feasible for solar sails [33]. Finally, the arrival attitude of the sail does not match the required attitude of the SSO. In order to address these discrepancies and improve the feasibility of the results, the collocation method of Section 5 is employed.

To initiate the 12^{th}-order Gauss-Lobatto collocation method, initial guesses are extracted from the trajectories in Fig. 11. A maximum transfer time interval of 3π to 6π is imposed with steps of π, on which the closest flyby with respect to GEO is selected as cutoff point, as shown in Fig. 11 by the white crosses. The arrival time on the SSO is furthermore discretized using 40 points equally spaced along the SSO, i.e., at intervals of $0.1\pi/\Omega_s$ in dimensionless units. This results in 160 possible initial guesses that are subsequently transferred into the collocation method, where the performance of all converged trajectories is shown in Fig. 13. On the horizontal axis, the transfer time of the trajectory is shown, while on the vertical axis the apogee altitude of the corresponding HEO can be seen. If the apogee altitude of the parking orbit increases, the maximum deliverable spacecraft mass to that orbit decreases as given in Fig. 6. Furthermore, the marker color describes the arrival time on the SSO. If a feasible trajectory with a perigee altitude of 250 km is found, it is shown as a circle in Fig. 13. Converged trajectories that also satisfy the HEO constraints (desired inclination and argument of perigee) are indicated with a triangle symbol. Finally, if also a feasible trajectory for spacecraft 2 is found, it is shown as a star in Fig. 13.

Out of 160 initial guesses, 36 transfers are found for which the perigee altitude constraint is satisfied. Other initial guesses failed to converge while reducing the altitude constraint using the stepwise approach. The quickest of these trajectories requires a transfer time of 39.6 days and arrives at the SSO at $t_{arr} = 0.125P_{SSO}$. After constraining the inclination and argument of perigee of the parking orbit to that of the HEO, 24 feasible trajectories remain, of which many have a close overlap with the round markers indicating that the perigee-altitude satisfying trajectories were already close to matching with a Soyuz HEO. Finally, 8 trajectories for spacecraft 2 were obtained. Note that after spacecraft 2 arrives in proximity of the SSO, an additional period of π/Ω_s is added as discussed in Section 7.4, which results in a constant increase in the transfer time of 14.84 days for spacecraft 2. The quickest trajectory for spacecraft 2 completes the transfer in 67.8 days, while the trajectory for spacecraft 1 with identical departure conditions arrives at the SSO in 53.0 days. These trajectories are shown in Fig. 14 with the corresponding control profile in Fig. 15.

Both trajectories follow the same path during the initial ballistic phase. After one day, the solar sail deploys and the two trajectories as well as the control history start to diverge. Over time, two flybys close to Earth are performed at altitudes higher than 10,000 km. A major difference between the trajectories can be seen by comparing the arrival conditions in Fig. 14(c) and 14(d), as both spacecraft wind onto the SSO at different locations along the SSO. The control for both spacecraft in Fig. 15 depicts an initial ballistic phase, followed by a rapidly varying control profile since no rotation rate is enforced at this point.

9.2. Active rotation rate constraint

In order to address the rapid changes in the control, this section provides the results when generating the same trajectories but with an active rotation rate constraint. These results are shown in Fig. 16.

By comparing Figs. 13 and 16, it can be seen that similar transfer times are found, irrespective of the activation of the maximum rotation rate constraint. However, the average apogee altitude is increased, indicating that constraining the rotation rate results in less energy efficient trajectories. This is expected as the locally optimal steering law requires large rotation rates and thus constraining the rotation rate results in a less optimal control. Furthermore, by enforcing a maximum rotation rate, the constraint violation is increased, requiring more iterations in the Gauss-Newton algorithm with respect to the unconstrained case. These iterations will cause the control profile to further diverge from the initial guess, which can cause either an increase or decrease in performance. As the results are feasible and not time-optimal, a direct comparison of the mission performance between Fig. 13 and 16 cannot be made. However, the results do show that multiple feasible solar-sail trajectories continue to exist while including a maximum rotation rate constraint of 20 deg/day.

Out of 9 trajectories found for spacecraft 2, the quickest result completes the transfer in 67.9 days, while the trajectory for spacecraft 1 with identical departure conditions completes its transfer in 53.1 days. These trajectories are shown in Fig. 17 with the corresponding control profile in Fig. 18. In order to determine the departure conditions, a value of $\phi_{2,0} = 135.4$ deg has been assumed in Eq. 16.

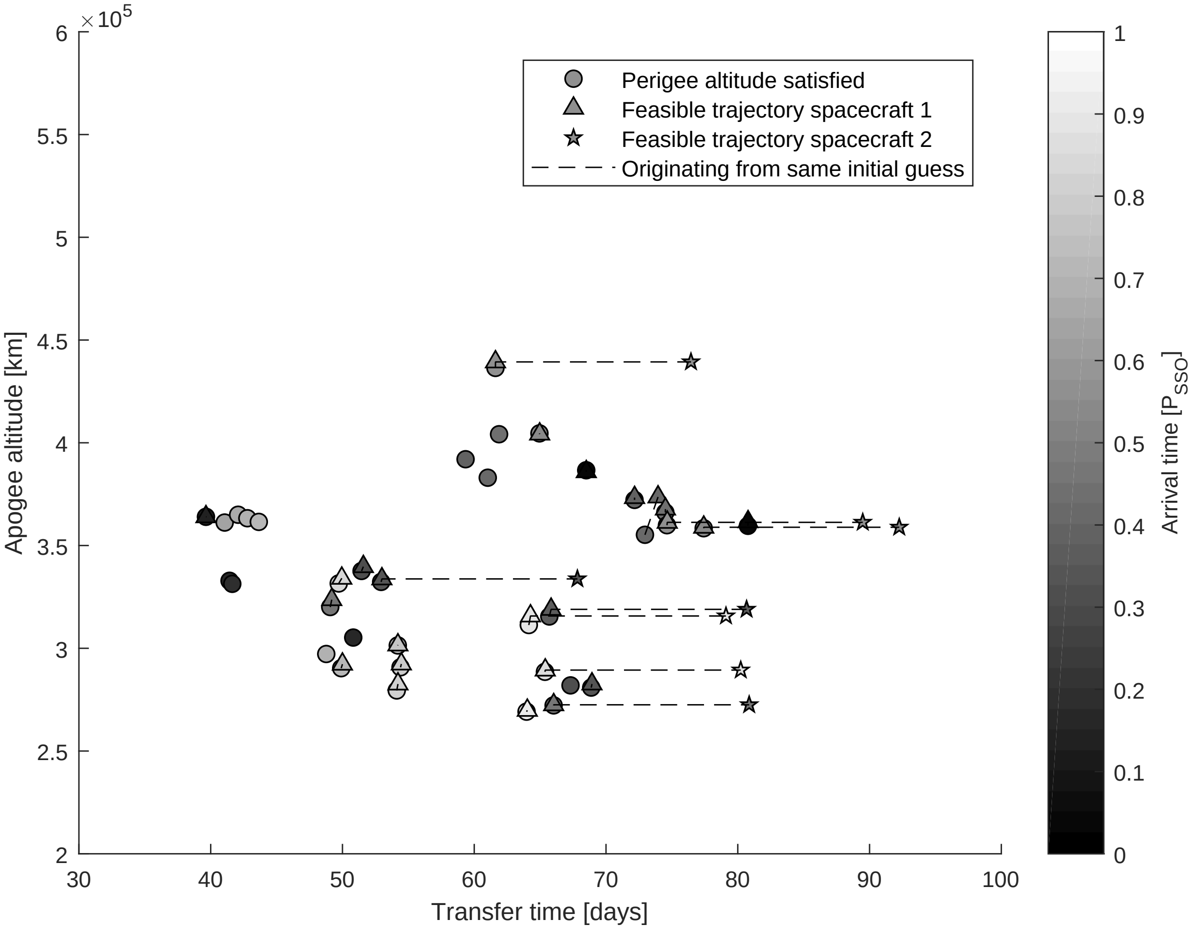

Fig. 13. Feasible transfer trajectories without rotation rate constraint.

The trajectories shown in Fig. 14 and 17 have a similar shape as they are both derived from the same initial guess. Major differences can be seen between Fig. 15 and Fig. 18, as the maximum rotation rate constraint produces a much smoother control profile. Note that δ is undefined for $\alpha = 0$, which allows for rapid changes in δ without violating the rotation rate constraint. These results show that solar-sail transfer trajectories are feasible in the Earth-Moon system without requiring long transfer times, low-altitude flybys or unrealistic solar-sail rotation rates.

9.3. Mass budget analysis

The transfer trajectories in Fig. 17 are used for the analysis on the mass budget. As mentioned in Section 7.5, two mass budgets are constructed, one for two large spacecraft utilizing the full Soyuz launch vehicle capacity, and another for two 10-kg CubeSats. Based on a HEO apogee altitude of 335,200 km (see Fig. 16), the Soyuz launcher can deliver two spacecraft of 1,160 kg each (see Fig. 6), which is comparable to the solar-sail spacecraft described in Ref. [34]. Table 5 contains the results of the preliminary mass budget. By estimating the required sail size, it is found that the 1160-kg mission requires a solar-sail area of 185.71 x 185.71 m^2 and allows for a 232.89 kg payload, while the 10-kg CubeSat mission requires a sail area of 17.24 x 17.24 m^2 and allows for a 2.01 kg payload.

10. CONCLUSIONS

This paper has proposed a methodology for the design of feasible transfers to solar-sail displaced libration point orbits in the Earth-Moon system. The methodology has been applied to reach a constellation of two solar-sail displaced vertical Lyapunov orbits at the L_2 point from where continuous coverage of the Aitken Basin, lunar South Pole, and Earth can be provided. A 12^{th}-order Gauss-Labotto collocation method and an adaptive mesh refinement method have been

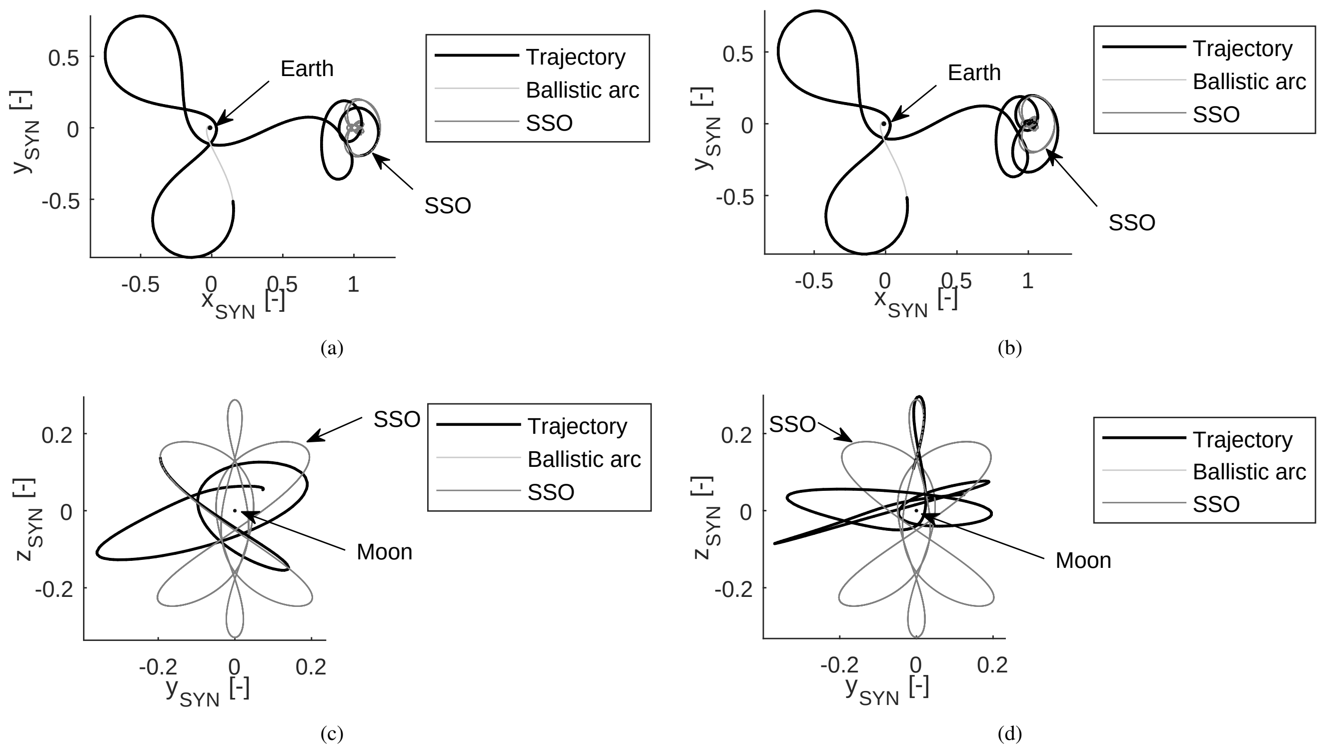

Fig. 14. Inactive rotation rate constraint: (a-b) Trajectories for spacecraft 1 (a) and 2 (b) projected on $(\hat{\mathbf{x}}_{SYN}, \hat{\mathbf{y}}_{SYN})$-plane. (c-d) Trajectories for spacecraft 1 (c) and 2 (d) projected on $(\hat{\mathbf{y}}_{SYN}, \hat{\mathbf{z}}_{SYN})$-plane.

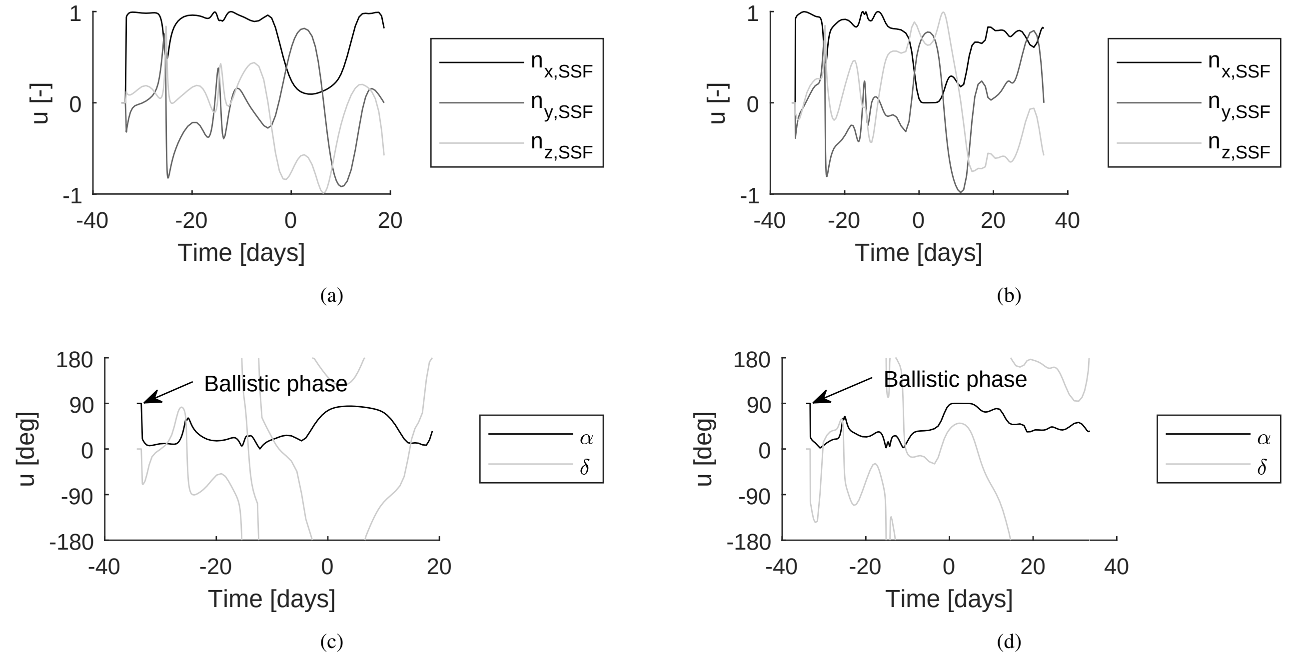

Fig. 15. Inactive rotation rate constraint: (a-b) Controls for spacecraft 1 (a) and 2 (b) expressed in Cartesian coordinates. (c-d) Controls for spacecraft 1 (c) and 2 (d) expressed in cone and clock angle.

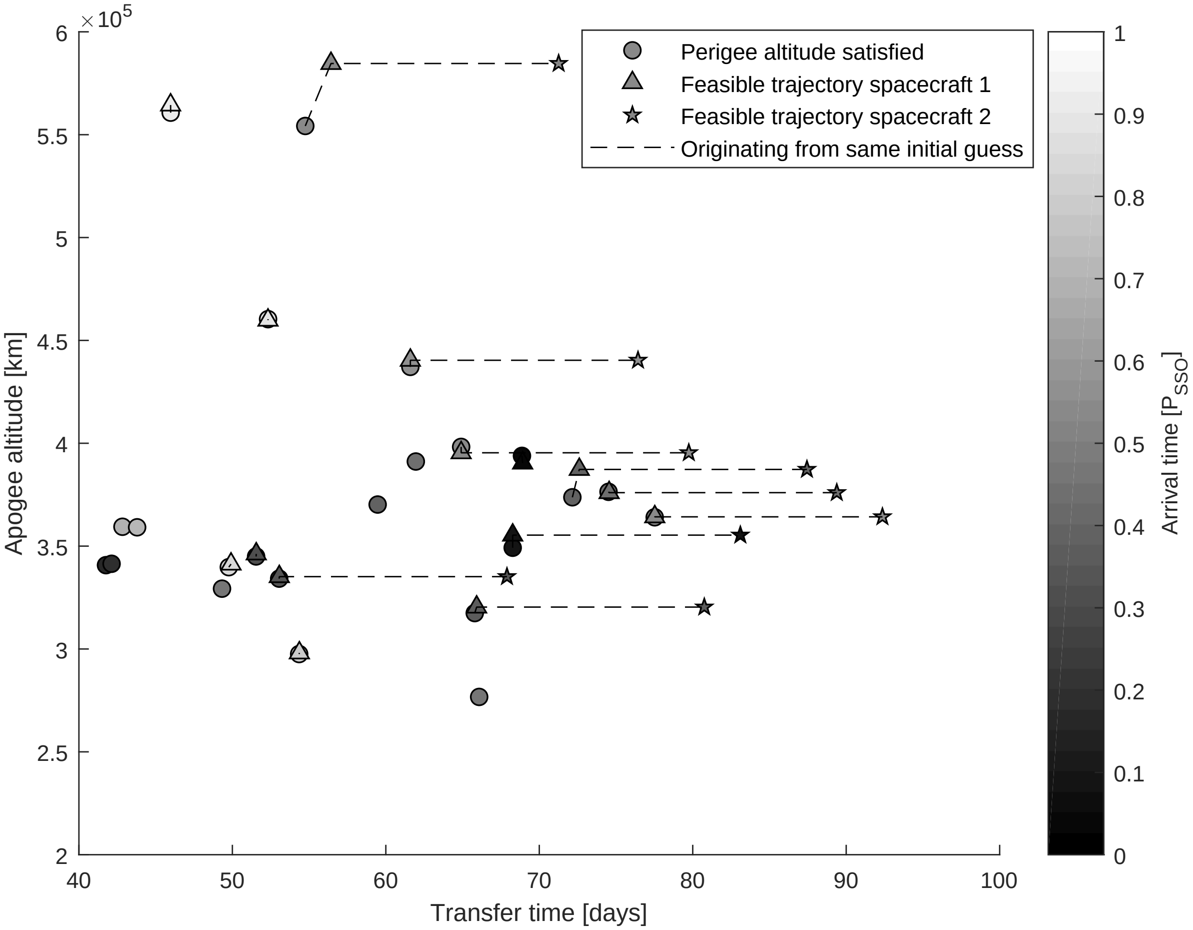

Fig. 16. Feasible transfer trajectories with active rotation rate constraint.

Table 5. Spacecraft subsystem mass estimations in kg for two mission scenarios.

Payload	2.01	232.89
Structure	1.56	181.04
Thermal	0.26	30.60
Power	2.34	271.13
TT&C	0.35	40.90
ADCS	0.51	58.65
Sail	2.97	344.90
Total	10.00	1160.00

applied to rewrite the trajectory problem to a nonlinear programming problem, which has consequently been solved using the Gauss-Newton algorithm. It has been shown that a range of path constraints, including altitude, solar-sail rotation rate and continuity constraints, can conveniently be implemented. Results have been produced in terms of two feasible trajectories with identical launch conditions that bring two spacecraft to their correctly-phased positions in the solar-sail displaced L_2 vertical Lyapunov constellation. During the transfers, the minimum altitudes with respect to Earth and the Moon are constrained to 3,000 km and four lunar radii, respectively, and the maximum rotation rate of the solar sail is constrained to 20 deg/day. The quickest transfer-time solution shows that the first spacecraft will reach its target orbit after a transfer time of 53.1 days, while the second spacecraft requires a transfer time of 67.9 days. A single Soyuz launch can deliver two 1160-kg spacecraft into these transfer trajectories. A subsystem mass estimation based on reference satellite data shows that the spacecraft can carry a 232.89-kg

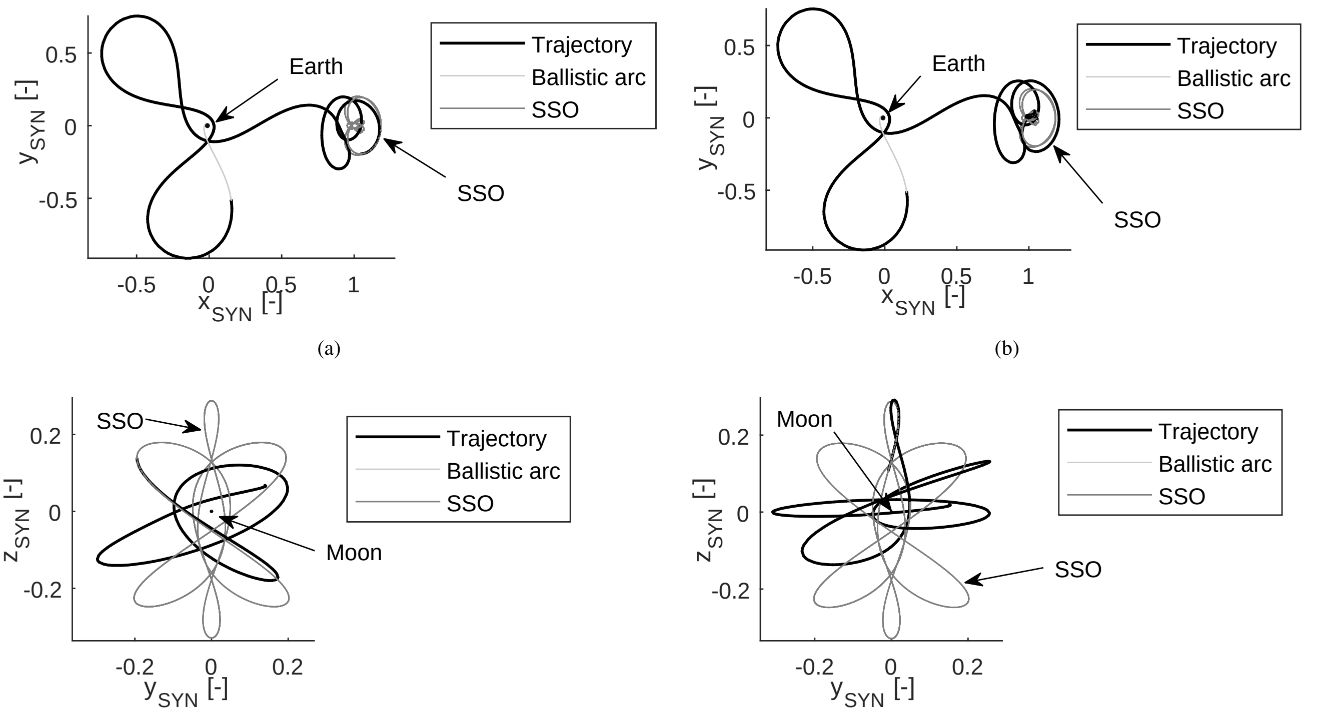

(a)

(b)

(c)

(d)

Fig. 17. Active rotation rate constraint: (a-b) Trajectories for spacecraft 1 (a) and 2 (b) projected on $(\hat{\mathbf{x}}_{SYN}, \hat{\mathbf{y}}_{SYN})$-plane. (c-d) Trajectories for spacecraft 1 (c) and 2 (d) projected on $(\hat{\mathbf{y}}_{SYN}, \hat{\mathbf{z}}_{SYN})$-plane.

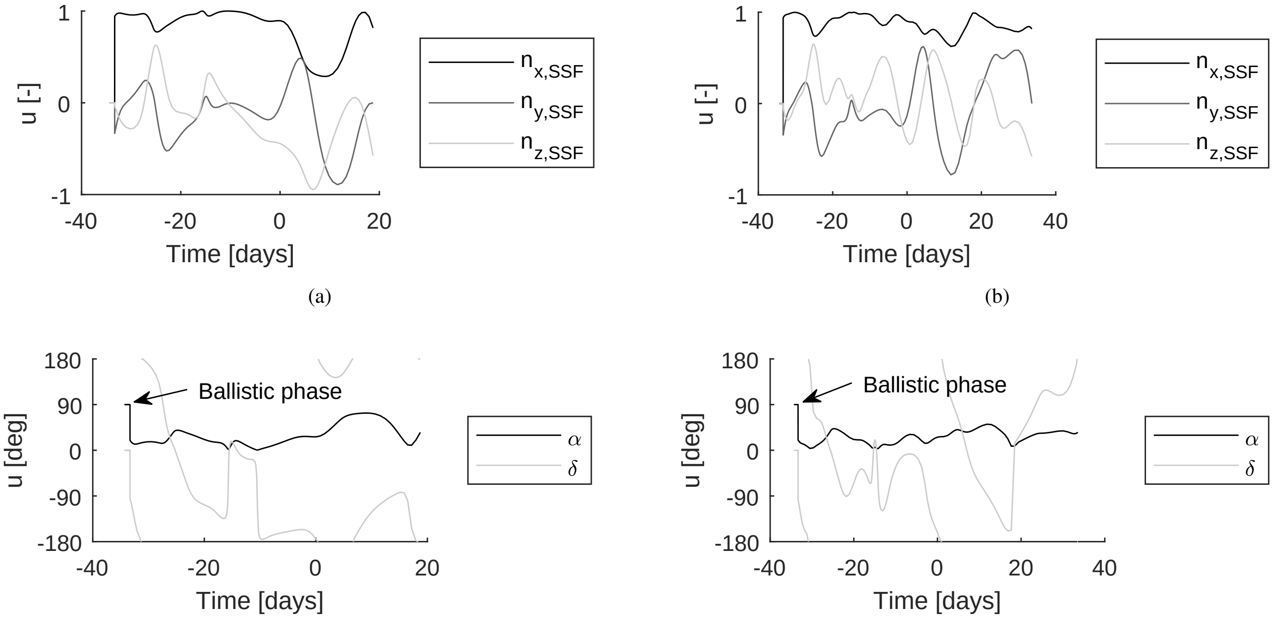

(a)

(b)

(c)

(d)

Fig. 18. Active rotation rate constraint: (a-b) Controls for spacecraft 1 (a) and 2 (b) expressed in Cartesian coordinates. (c-d) Controls for spacecraft 1 (c) and 2 (d) expressed in cone and clock angle.

payload and requires a solar-sail area of 185.71 x 185.71 m^2. Alternatively, a 10-kg CubeSat mission would be able to carry a 2.01-kg payload per CubeSat requiring a 17.24 x 17.24 m^2 solar sail. These results show that solar-sail transfer trajectories in the Earth-Moon system are feasible without requiring long transfer times, low-altitude flybys or unrealistic solar-sail rotation rates.

11. REFERENCES

[1] L. Johnson, M. Whorton, A. Heaton, R. Pinson, G. Laue, and C. Adams, "NanoSail-D: A solar sail demonstration mission," *Acta Astronautica*, vol. 68, pp. 571–575, 2011.

[2] Y. Tsuda, O. Mori, R. Funase, H. Sawada, T. Yamamoto, T. Saiki, T. Endo, K. Yonekura, H. Hoshino, and J. Kawahuchi, "Achievement of IKAROS - Japanese deep space solar sail demonstration mission," *Acta Astronautica*, vol. 82, pp. 183–188, 2013.

[3] B. Greeson E. Vaughn J. Chute R. Spencer D. A. Ridenoure R. W. Munakata R. Wong S. D. Diaz A. Stetson D. A. Foley J. D. Bellardo J. M. Plante B Betts, B. Nye, "Lightsail 1 mission results and public outreach strategies," in *The Fourth International Symposium on Solar Sailing*, Kyoto, Japan, Jan. 2017.

[4] C. McInnes, *Solar Sailing: Technology, Dynamics and Mission Applications*, Springer-Verlag, Berlin, Germany, 2nd edition, 2004.

[5] H. Baoyin and C. McInnes, "Solar sail halo orbits at the Sun-Earth artificial L1-point," *Celestial Mechanics and Dynamical Astronomy*, vol. 94, pp. 155–171, 2006.

[6] T.J. Waters and C.R. McInnes, "Periodic orbits above the ecliptic in the solar-sail restricted three-body problem," *Journal of Guidance, Control, and Dynamics*, vol. 30, no. 3, pp. 687–693, 2007.

[7] P. Verrier, W. Waters, and J. Sieber, "Evolution of the L1 halo family in the radial solar sail circular restricted three-body problem," *Celestial Mechanics and Dynamical Astronomy*, vol. 120, no. 4, pp. 373–400, 2014.

[8] J. Heiligers, M. Macdonald, and J.S. Parker, "Extension of Earth-Moon libration point orbits with solar sail propulsion," *Astrophysics and Space Science*, vol. 361, no. 7, jun 2016.

[9] J. Heiligers, S. Hiddink, R. Noomen, and C.R. McInnes, "Solar sail Lyapunov and halo orbits in the Earth-Moon three-body problem," *Acta Astronautica*, vol. 116, pp. 25–35, 2015.

[10] J. Heiligers, J.S. Parker, and M. Macdonald, "Novel solar-sail mission concepts for high-latitude Earth and lunar observation," *Journal of Guidance, Control, and Dynamics*, vol. 41, no. 1, pp. 212–230, jan 2018.

[11] I.A. Crawford, M. Anand, C.S. Cockell, H. Falcke, D.A. Green, R. Jaumann, and M.A. Wieczorek, "Back to the Moon: The scientific rationale for resuming lunar surface exploration," *Planetary and Space Science*, vol. 74, no. 1, pp. 3–14, dec 2012.

[12] V.L. Coverstone and J.E. Prussing, "Technique for escape from geosynchronous transfer orbit using a solar sail," *Journal of Guidance, Control, and Dynamics*, vol. 26, no. 4, pp. 628–634, jul 2003.

[13] A. Das-Stuart and K. Howell, "Solar sail transfers from Earth to the lunar vicinity in the circular restricted problem," in *AIAA/AAS Astrodynamics Specialist Conference*, Vail, CO, USA, aug 2015.

[14] M. T. Ozimek, D. J. Grebow, and K. C. Howell, "Design of solar sail trajectories with applications to lunar south pole coverage," *Journal of Guidance, Control, and Dynamics*, vol. 32, no. 6, pp. 1884–1897, nov 2009.

[15] A. Herman, *Improved Collocation Methods with Application to Direct Trajectory Optimization*, Ph.D. thesis, University of Illinous at Urbana-Champaign, 1995.

[16] J.F.C. Herman, *Improved Collocation Methods to Optimize Low-Thrust, Low-Energy Transfers in the Earth-Moon System*, Ph.D. thesis, University of Colorado at Boulder, 2015.

[17] J.T. Betts, "A survey of numerical methods for trajectory optimization," *Journal of Guidance, Control, and Dynamics*, vol. 21, no. 2, pp. 193–207, mar 1998.

[18] C. de Boor, "Good approximation by splines with variable knots," in *Spline Functions and Approximation Theory*, vol. 363, pp. 57–72. Birkhuser Basel, 1973.

[19] A. Bjorck, *Numerical Methods for Least Squares Problems*, Society for Industrial and Applied Mathematics, jan 1996.

[20] D. Williams, "Planetary fact sheet - metric," Online, nov 2015.

[21] R.H. Battin, *An Introduction to the Mathematics and Methods of Astrodynamics, Revised Edition*, AIAA Eduction Series. American Institute of Aeronautics and Astronautics, Inc., Reston, USA, 1999.

[22] M. Ceriotti and C.R. McInnes, "Generation of optimal trajectories for Earth hybrid pole sitters," *Journal of Guidance, Control, and Dynamics*, vol. 34, no. 3, pp. 847–859, may 2011.

[23] E. Perez, *Soyuz user's manual*, Arianespace, 2 edition, mar 2012.

[24] V. Chobotov, *Orbital Mechanics*, AIAA, 3rd edition, 2002.

[25] R. Bate, D. Mueller, and J White, *Fundamentals of Astrodynamics*, Dover Publications, New York, USA, 1st edition, 1971.

[26] A.L. Herman and B.A. Conway, "Direct optimization using collocation based on high-order Gauss-Lobatto quadrature rules," *Journal of Guidance, Control, and Dynamics*, vol. 19, no. 3, pp. 592–599, may 1996.

[27] J.R.R.A. Martins, P. Sturdza, and J.J. Alonso, "The complex-step derivative approximation," *ACM Transactions on Mathematical Software*, vol. 29, no. 3, pp. 245–262, sep 2003.

[28] T.A. Davis, *UMFPACK User Guide*, SuiteSparse, 5.7.6 edition, May 2016.

[29] R. D. Russell and J. Christiansen, "Adaptive mesh selection strategies for solving boundary value problems," *SIAM Journal on Numerical Analysis*, vol. 15, no. 1, pp. 59–80, feb 1978.

[30] L.F. Shampine and M.W. Reichelt, "The MATLAB ODE suite," *SIAM Journal on Scientific Computing*, vol. 18, no. 1, pp. 1–22, jan 1997.

[31] J. Wertz, *Space Mission Analysis and Design*, Space Technology Library, Microcosm press/Kluwer Academic Publishers, El Segundo, California, USA, 3rd edition edition, 1999.

[32] B. Dachwald, "Optimal solar sail trajectories for missions to the outer Solar System," *Journal of Guidance, Control, and Dynamics*, vol. 28, no. 6, pp. 1187–1193, nov 2005.

[33] G. Mengali and A.A. Quarta, "Near-optimal solar-sail orbit-raising from low Earth orbit," *Journal of Spacecraft and Rockets*, vol. 42, no. 5, pp. 954–958, sep 2005.

[34] J. Heiligers, T. van den Oever, M. Ceriotti, P. Mulligan, and C. McInnes, "Continuous planetary polar observation from hybrid pole-sitters at Venus, Earth, and Mars," in *The Fourth International Symposium on Solar Sailing*, Kyoto, Japan, Jan. 2017.